UC Berkeley
UC Berkeley Electronic Theses and Dissertations

Title
Bone Strength Multi-axial Behavior - Volume Fraction, Anisotropy and Microarchitecture

Permalink
https://escholarship.org/uc/item/08j3c24w

Author
Sanyal, Arnav

Publication Date
2013

Peer reviewed|Thesis/dissertation

eScholarship.org Powered by the California Digital Library
University of California

Bone Strength Multi-axial Behavior – Volume Fraction, Anisotropy and Microarchitecture

By

Arnav Sanyal

A dissertation submitted in partial satisfaction of the

requirements for the degree of

Doctor of Philosophy

in

Engineering – Mechanical Engineering

in the

Graduate Division

of the

University of California, Berkeley

Committee in charge:

Professor Tony M. Keaveny, Chair
Professor Panayiotis Papadopoulos
Professor Mohammad R.K. Mofrad
Professor Song Li

Fall 2013

Bone Strength Multi-axial Behavior – Volume Fraction, Anisotropy and Microarchitecture

© 2013
by
Arnav Sanyal

ABSTRACT

Bone Strength Multi-axial Behavior- Volume Fraction, Anisotropy and Microarchitecture

by

Arnav Sanyal

Doctor of Philosophy in Engineering – Mechanical Engineering

University of California, Berkeley

Professor Tony M. Keaveny, Chair

Trabecular bone is a major load-bearing tissue in the musculoskeletal system and is subjected to various multi-axial loads *in vivo*. For example, in the vertebral body, the trabecular bone is primarily subjected to uniaxial loads, in the proximal femur, trabecular bone is subjected to biaxial loads i.e. loads oriented at two mutually perpendicular directions, in distal radius, the trabecular bone can subjected to shear loads due to off-axis loading during a traumatic event. Understanding the multi-axial strength and underlying tissue-level failure mechanisms of human trabecular bone is of great clinical and scientific importance since age-related osteoporotic fractures primarily occur at trabecular bone sites, such as the hip, spine and wrist. With the onset of osteoporosis, there is an increase in porosity and deterioration of the microarchitecture of trabecular bone, which results in increased fragility and fracture susceptibility of trabecular bone.

Using high-resolution, micro-CT based nonlinear finite element models, we investigated the strength of trabecular bone under compression, shear, biaxial and multi-axial loading conditions. Under uniaxial loading, it was shown that the variation in both compressive and shear strength was primarily attributed to the volume fraction of the trabecular bone, but the observed scatter in the ratio of the shear and compressive strength was attributed to heterogeneity and anisotropy of the trabecular microarchitecture. At the tissue-level, it was shown that shear loading leads to predominantly tensile tissue failure unlike compression loading that makes trabecular bone much weaker under shear loading. Under biaxial loading, it was shown that the yield strength varied with both volume fraction and anisotropy, and most of the variation in biaxial strength could be primarily attributed to similar variation of the uniaxial strengths with minor variations due to trabecular microarchitecture. Based on these results, the complete multi-axial yield strength behavior of trabecular bone was investigated for over 200 multi-axial load cases. A new yield strength criterion was then formulated in the six-dimensional strain space to mathematically characterize the multi-axial failure criterion of human trabecular bone.

The research presented in this dissertation has provided considerable insight into the variation of both apparent-level strength and the tissue-level failure mechanisms of trabecular bone under various loading conditions. The role of bone volume fraction, anisotropy and microarchitecture on the uniaxial and multi-axial strength has been outlined. A multi-axial failure criterion has been formulated which can be used to non-invasively predict the strength of whole bones of osteoporotic patients using clinical CT scans.

TABLE OF CONTENTS

LIST OF FIGURES

LIST OF TABLES

ACKNOWLEDGEMENTS

First, I would like to thank my Ph.D. advisor, Tony Keaveny for introducing me to the field of biomechanics and providing me the opportunity to conduct my doctoral research in the Orthopaedic Biomechanics Lab. He has been a great research advisor, providing guidance and encouragement throughout my graduate studies. I am grateful to Professors Panayiotis Papadopoulos, Mohammad Mofrad and Song Li for serving on my dissertation committee. I would like to thank Aaron Fields and Sarah Easley for teaching me everything that I needed to get my research done. I would also like to thank Shashank Nawathe for being a great company in the lab for the major part of my graduate studies. I also thank a number of undergraduate students researchers – Amanda Eng, Derek Lew, Eunice Fu, Ivana Yi, Joanna Scheffelin, Justine Velasco, Kevin Chow, Kevin Ma, Kim Penamora, Ruben Maldonado and Sebastian Ruf, who have worked with me in various projects and assisted me in my research. I would like to acknowledge Andy Burghardt at UCSF for his assistance with the micro-CT imaging of the bones. I would also like to acknowledge the National Institutes of Health for providing funding support for this research. I would also like to thank the Department of Mechanical Engineering for providing financial support through fellowships and teaching assistantships. Finally, I would like to thank my parents and sister for their emotional support throughout my graduate studies.

1. INTRODUCTION

Bone is the major load bearing tissue in the musculoskeletal system. Based on the level of porosity, bone is characterized as either cortical or trabecular (**Figure 1-1**). Cortical bone has porosity of 30% or less and is found in the diaphysis region of long bones. Trabecular bone is the spongy and highly porous (porosity = 60-95%) bone found at the end of long bones such as the proximal femur, in the center of the vertebra, and in flat bones such as the skull. Functionally, trabecular bone supports the articular surface of joints for the transfer of muscle and joint loads along the long bone. The porous structure provides shock absorption, allows nutrients to easily diffuse to the bone cells and serves a primary site for production of red blood cells. The differences in functional requirements of trabecular bone at different anatomic sites are reflected in differing levels of porosity and arrangements of the individual trabeculae, or trabecular microarchitecture.

The structure and mechanical properties of trabecular bone changes in response to biological and mechanical stimuli in the body. This process, called bone remodeling, occurs continually to repair, replace, and remove damaged or aging bone tissue. Besides the biological stimuli, mechanical loading also plays an important role in bone remodeling process, which can change the bone structure and its mechanical properties. With onset of osteoporosis with aging, due to imbalance in bone remodeling, there is a decrease in bone mass and deteriorated microarchitecture of trabecular bone that leads to enhanced bone fragility and increased risk of fracture (**Figure 1-2**). The mechanical properties of trabecular bone are therefore, of great clinical importance because of the role it plays in the etiology of osteoporosis and age-related fractures. Moreover, due to traumatic loading or surgical procedures such as bone grafts and joint arthoplasty, can generate in vivo multi-axial loads in trabecular bone. This dissertation describes the failure of trabecular bone under compression, shear and various multi-axial loading conditions. In the remainder of this chapter, a description of trabecular bone is presented, followed by a review of its mechanical properties. A review of failure theories that have been applied to trabecular bone is then presented, focusing on multi-axial theories. Lastly, a detailed description of the objectives and scope of this dissertation is given.

1.1 Trabecular Bone Structure and Morphology

Trabecular bone is composed of a lattice like network of microstructural struts or trabeculae, which form a three-dimensional, interconnected, open porous cellular solid type of material. The trabeculae are composed of the trabecular tissue material, which is a composite of hydroxyapatite, collagen, water and other proteins arranged in the form of packets of lamellar bone. The morphology of the trabecular structure can vary greatly within individuals and with age and anatomic site. Most of the variation in morphology can be described by bone volume fraction (BV/TV, the fraction of the total volume that is occupied by trabecular hard tissue) or apparent bone density (ρ, the ratio of bone mass to total volume). These two properties are related by the density of the trabecular tissue ($\rho_{tissue} = \rho$ / BV TV), which is relatively constant for healthy adults = 2 g/cc [1].

In addition to BV/TV, several parameters have been developed to quantify the trabecular microarchitecture [2]. The most commonly used descriptor of the trabecular architecture is the fabric tensor, a symmetric second rank tensor that characterizes the structural anisotropy of trabecular bone [3]. The fabric tensor is constructed from volumetric material distribution measures which are taken at various angles within a trabecular bone specimen in three-dimensions. The most common measure used to construct the fabric tensor is the mean intercept length (MIL) [4]. The eigenvalues of the fabric tensor quantify the degree of anisotropy (DA) of the specimen [5] and the associated eigenvectors are the directions of principal material orientation. Structures with a DA near one are relatively un-oriented, and increasing values of DA represent increasing levels of directional orientation. The morphological anisotropy based on the fabric tensor has been related to the mechanical or elastic anisotropy of the trabecular structure in various studies [6].

Besides the fabric tensor, other architectural indices such as the mean trabecular separation (Tb.Sp), trabecular thickness (Tb.Th), trabecular number (Tb.N), Structure Model Index (SMI) and connectivity density (Conn.Dn) have been developed to describe the morphology of the trabeculae [2]. Connectivity is a measure of structural redundancy of the trabecular structure and represents the maximal number of branches that can be broken before a trabecular structure is separated into two parts [7]. Tb.Th and Tb.Sp are defined as the average thickness of an object volume and the average thickness of a pore space, respectively. Tb.N is defined as the inverse of the average distance between object mid-axes, and is thus conceptually related to Tb.Sp. SMI describes the overall convexity/concavity of the trabecular surfaces with respect to interior points within the trabeculae [8]. Flat plate-like structures have an SMI of zero, whereas ideal cylindrical rods have an SMI of three. With advances in imaging technology and the availability of micro-computed tomography [9], these architectural indices have become readily available since they are automatically calculated using three-dimensional high-resolution images of trabecular bone specimens [10]. More recently, an individual trabeculae segmentation (ITS) technique [11] has been developed, which spatially decomposes the trabecular bone microstructure into individual trabecular plates and rods.

1.2 Trabecular Bone Mechanical Properties

The mechanical properties of trabecular bone has clinical relevance since most age-related fractures most frequently occur in anatomic sites composed of trabecular bone such as the proximal femur (hip), the vertebrae (spine) and the distal radius (wrist). In addition, joint replacement surgery involves implanting fixtures into regions of trabecular bone, thereby subjecting trabecular bone to complex stress states. The mechanical property of trabecular bone specimen, which is made up of many trabecular struts and has dimensions > 1mm, are called the apparent-level properties. The apparent properties depend on the material properties of bone tissue matrix, the relative density i.e the bone volume fraction and microarchitecture. The trabecular microstructure is typically oriented, such that there is a “grain” direction (called the principal material direction) along which elastic stiffness and strength are greatest. This microstructural

directionality gives trabecular bone anisotropy of elastic properties and is generally considered to be orthotropic [12]. Further, the orthotropic elastic properties of trabecular bone have been related to the trabecular microarchitecture parameters [3, 6].

Trabecular bone failure properties have been investigated extensively for uniaxial loading. The uniaxial strength of trabecular bone is anisotropic with apparent elastic modulus and with density BV/TV [13-15]. In addition, trabecular microarchitecture measures have been shown to improve the density-strengths correlations [16]. Despite the substantial variations that exist in yield stresses, the yield strains for trabecular bone measured using the 0.2% offset method are found to be uniform within an anatomic site [14, 17]. However under off-axis loading, i.e. when loaded oblique to the principal material direction, the yield strains are heterogeneous [18].

A few studies have investigated the multi-axial failure properties of trabecular bone. Combined axial-torsion loading experiments on bovine trabecular bone showed that under combined tension and shear, failure occurs when the principal strain reached the uniaxial tensile yield strain [19]. However, under combined compression and shear loading the principal strain at failure was greater than the uniaxial compressive yield strain. While this behavior was better captured by a cellular solid theory based yield criterion, only one axial-shear load plane was discussed and the results cannot be easily generalized for other combined loading cases. Theories developed for composites such as the Tsai-Wu failure criterion [20] have also been suggested and formulated for trabecular bone [21] with fabric-based anisotropy. However, this theory was found to be too restrictive for bovine trabecular bone. It was shown that specimens loaded under triaxial compression yielded nearly at their uniaxial yield stresses [22], while the Tsai-Wu criterion dictates a larger reduction in strength for triaxial loading. This can be explained by the uncoupling of the yield behavior under multiaxial loads for trabecular bone [23]. A complete three-dimensional yield criterion was formulated for high-density trabecular bone from femoral neck [24]. Others research groups have proposed a piecewise Hill's criterion [25] and fit data generated from uniaxial compression, tension, torsion and triaxial compression on specimens from various anatomic sites [26]. More recently, a fabric-based Tsai-Wu criteria was formulated for trabecular bone specimens from the verterbral body [27]. A few other studies that model trabecular bone as a cellular solid or foam, have investigated the crushable foam plasticity formulation to characterize the pressure dependent yield behavior of trabecular bone [28-30].

1.3 Objectives and Scope of the Dissertation

The overall goals of this dissertation research is to investigate the strength behavior of trabecular bone under different loading conditions such as compression, shear, torsion and multi-axial loading conditions and formulate a generic multi-axial failure criterion of any human trabecular bone. High-resolution micro-CT-based finite element modeling will be used on human trabecular bone specimens to accomplish these goals.

In Chapter 2, the strength of trabecular bone under shear loading is investigated and is compared against strength under compression loading. The underlying tissue-level failure mechanisms, the tissue-level failure type and the effects of large deformations are discussed. To date, very few studies have investigated the shear behavior of human trabecular bone, which might be relevant for loading experienced by trabecular bone at bone-implant interface. The study also explores strength under torsion loading, which has been often used to evaluate shear strength of trabecular bone experimentally.

In Chapter 3, the strength of trabecular bone under biaxial loading is investigated. Such loading might be relevant for hip fractures in the proximal femur. The relative roles of volume fraction, anisotropy and microarchitecture, on the parameters of the biaxial strength are discussed. Specifically, the role of anisotropy independent of bone volume fraction is emphasized. In addition, the tissue-level failure mechanisms are discussed for two biaxial loading cases that typically occur in the proximal femur.

In Chapter 4, a new multi-axial yield criterion for human trabecular bone is proposed that can be used in continuum-level whole bone models. High-resolution finite element models are used to analyze hundreds of multi-axial loading scenarios providing failure data that would be impossible to obtain experimentally. The multi-axial strength data is normalized by the uniaxial strength to eliminate the variations due to bone volume fraction and anisotropy and a mathematical yield criterion for trabecular bone is developed using these normalized data in a quartic functional form.

Finally, conclusions of the research are presented in Chapter 5, including a discussion of directions of future research.

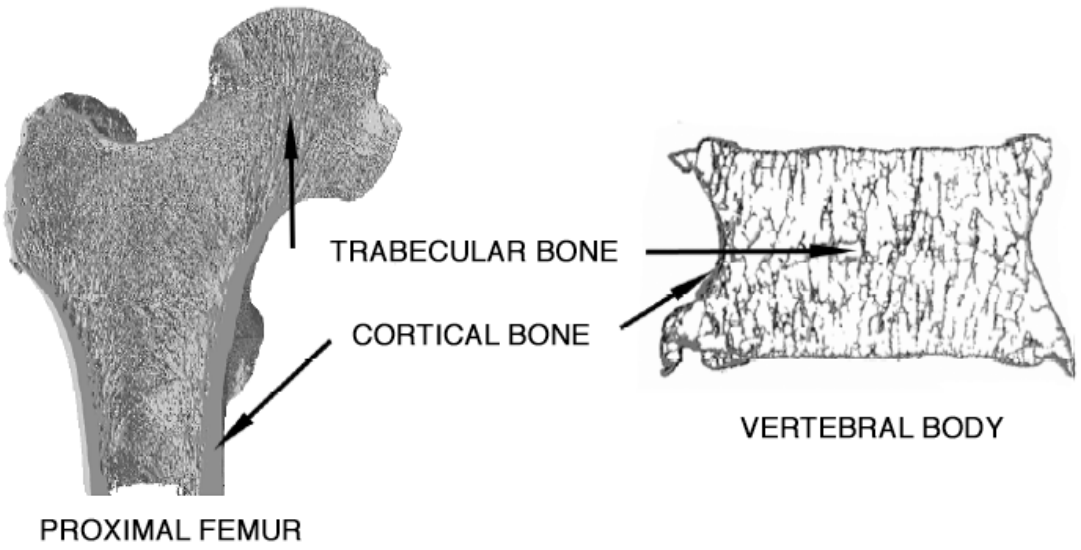

Figure 1-1: Internal morphology of a human proximal femur (hip) and a thoraric vertebral body (spine) show the typical arrangement of cortical and trabecular bone.

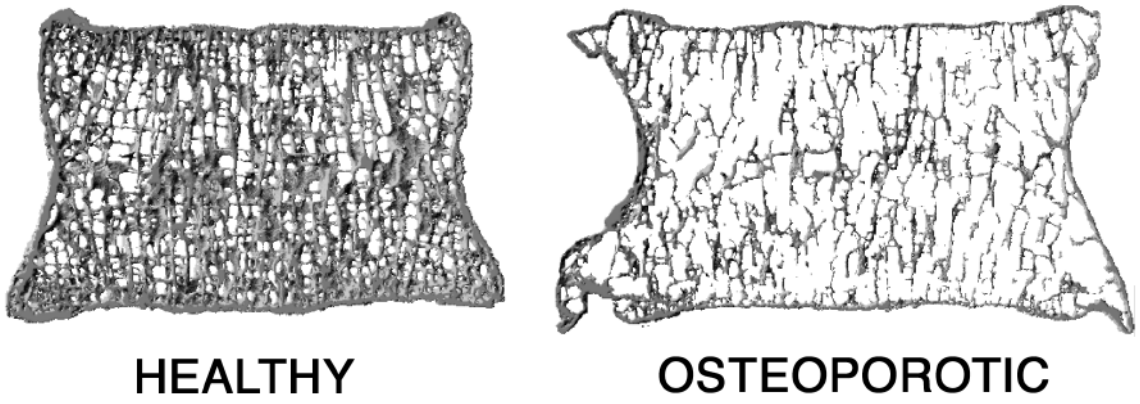

Figure 1-2: Frontal slices through the vertebra of a healthy individual and one from an elderly, osteoporotic individual illustrating the decrease in bone mass and deterioration of trabecular microarchitecture with osteoporosis

2. SHEAR STRENGTH BEHAVIOR OF HUMAN TRABECULAR BONE

2.1. Introduction

Since trabecular bone is thought to be primarily adapted to sustain compressive loads along its main trabecular orientation, most focus to date in biomechanical studies of human trabecular bone has been placed on understanding its compressive strength behavior [13, 31] [14, 32, 33] [15, 34]. However, obliquely oriented external loads can generate substantial shear stress within a bone with respect to the main trabecular orientation, which may be relevant for understanding bone trauma, including hip fracture etiology [35] [36, 37]. Likewise, large shear stresses can develop near bone-implant interfaces, which may influence orthopaedic implant loosening [38]. In analyzing such situations, the shear strength of trabecular bone may be equally or even more relevant than its compressive strength.

To date, only a few studies have addressed the apparent-level shear strength behavior of trabecular bone, particularly for humans [39] [19, 35, 40-42] [26, 43, 44]. It has been proposed that the structure-function relations may differ between compression vs. shear loading because trabecular bone may maintain structural integrity for habitual (compressive) loading, but may be degraded for non-habitual (shear) loading, particularly for individuals prone to fracture [45, 46]. Similarly, while the shear strength of bovine trabecular bone may be low because of pronounced bending of individual trabeculae [19], little is known about the associated shear failure mechanisms in human trabecular bone—which may differ from bovine mechanisms because of inter-species differences in bone volume fraction and micro-architecture. Thus, to further understanding of the shear strength behavior of human trabecular bone, we sought here to compare the apparent-level shear and compressive strengths of a wide range of human trabecular bone and to explore the underlying failure mechanisms.

2.2. Methods

A total of 65 human cadaver specimens of trabecular bone, from four anatomic sites, were initially chosen for this analysis. These specimens, taken from prior studies in our laboratory [14, 17, 47], were originally machined as 8 mm-diameter cylindrical cores, along their principal trabecular orientation, and were scanned at a spatial resolution of 10–22 mm using either micro-CT (n=44; μCT 20; Scanco Medical AG, Bruttisellen, Switzerland) or serial milling (n=21) [48]. Standard trabecular microarchitecture parameters [10, 49] were available for all specimens that were scanned with micro-CT. A subset (n=22) of these specimens were also mechanically tested to failure in compression. For the purposes of this study, one voxel-based finite element model was generated for each specimen, the model comprising a 5 mm cube (**Figure 2-1**) that was virtually extracted from the images of the central portion of the larger cylindrical specimen. An element size of 66 μm was used for the femoral neck specimens, and 22 μm for the greater trochanter, proximal tibia and vertebral body specimens. These resolutions were based on convergence requirements that the ratio of mean trabecular thickness to element

size be at least 4 [50, 51]. Individual models had between about 1–5 million elements. To ensure that these extracted cube specimens were adequately aligned (within $\pm 10^0$ of the principal trabecular orientation), six uniaxial linear elastic finite element analyses were performed on each specimen to calculate the Euler angles of misalignment [52]. Eight specimens from the greater trochanter and three specimens from the proximal tibia were eliminated because of misalignment. This resulted in a final cohort of 54 specimens, which together spanned four anatomic sites, were taken from 44 different cadavers, and displayed a wide range (0.06–0.38) of bone volume fraction (**Table 2-1**). For this final cohort, the trabecular microarchitecture parameters were available only for the specimens that were imaged using micro-CT (n=39).

Two non-linear finite element analyses were performed on each specimen to calculate both the apparent-level shear and compressive yield strengths. In all analyses, all finite elements were assigned the same hard tissue material properties having an isotropic elastic modulus of 18.0 GPa, a Poisson's ratio of 0.3, and a rate-independent elastic-plastic material model [53]. The models also included kinematic non-linearity (''large-deformation'' effects), which are important to include for specimens having low bone volume fraction [47]. In the voxel-level constitutive model, tissue-level failure was allowed to occur only by tissue-level yield. Such yielding comprised a modified von-Mises criterion with tension-compression strength asymmetry, which was achieved by introducing pseudo kinematic hardening to shift the yield envelope. The tissue-level yield strains of 0.33% in tension and 0.81% in compression were chosen based on a prior calibration study [47]. This overall implementation provided excellent agreement (Y~X, R^2=0.96) for compressive apparent-level yield strength between model and experiment for the 22 specimens for which we had both mechanical testing and finite element yield strength data (**Figure 2-2**). For each model, displacement boundary conditions were applied to impose uniaxial shear stress for shear strength assessment (**Figure 2-1b**) and uniaxial compressive stress for compressive strength assessment (**Figure 2-1c**). All analyses were performed using a highly scalable, implicit parallel finite element framework, Olympus [54] on a Sun Constellation Linux Cluster (Ranger; Texas Advanced Computing Center, TX, USA), each analysis requiring about 100 CPU hours.

The main outcomes from these analyses were the apparent-level shear and compressive yield strengths, which were obtained using an offset of 0.2% strain applied to the computed apparent-level stress–strain curves. To gain insight into tissue-level failure mechanisms, the proportion of yielded tissue (equivalent to number of elements for which the maximum or minimum principal stress at the element centroid had exceeded the tissue-level tensile or compressive yield strength, respectively, divided by total number of elements) and the tissue-level yield mode (tensile or compressive) was calculated at the apparent-level 0.2% offset yield point. For all yielded elements, those elements having a ratio of maximum principal stress to tensile strength of greater than the ratio of minimum principal stress to compressive strength were considered to yield in tension at the tissue level; otherwise they were considered to yield in compression at the tissue level. For our statistical analyses, non-linear and general linear regression modeling (JMP, Version 9.0.0, SAS Institute Inc., Cary, NC) was used to determine the

dependence of the various apparent-level and tissue-level outcomes on apparent-level loading mode and on bone volume fraction, anatomic site, and microarchitecture.

In a sub-study, we used the computational techniques described above to measure the yield strength of 15 cylindrical cores (8 mm diameter, 12–15 mm length, BV/TV=0.19±0.10, 0.07–0.38) under torsion loading. These cores were chosen from the original image set of the 54 cubes specimens. The nodes on the bottom face of the cores were fully constrained and a rotational displacement was applied on the nodes of the top face equivalent to 1.5% apparent engineering shear strain. The shear stress was calculated from the apparent-level torque vs. angle of twist curve using the following equation [55]:

$$\tau = \frac{1}{2\pi r^3}\left[\theta\frac{dT}{d\theta} + 3T\right]$$

where T is the calculated torque, r is the radius of the specimen and y is the angle of twist per unit length. The term dT/dθ was determined by fitting a fifth-degree polynomial to the torque vs. angle of twist curve.

2.3. Results

Both the apparent-level shear (R^2=0.95) and compressive (R^2=0.97) yield strengths depended on bone volume fraction in a non-linear fashion, each relation having an exponent of 1.7 (**Figure 2-3**). Because the relation between apparent-level yield strength and bone volume fraction relation did not depend on anatomic site (p=0.55 for shear; p=0.09 for compression), data from the four different anatomic sites were pooled in most subsequent results. Both the shear and compressive yield strengths were highly correlated with almost all the microarchitecture parameters (**Table 2-2**), which was expected since most microarchitecture parameters generally have high correlation with bone volume fraction [10]. The apparent-level yield strain decreased slightly with bone volume fraction for shear loading (R^2=0.07, p=0.05) but clearly increased for compressive loading (R^2=0.42, p<0.001).

With the exception of one specimen, the shear strength was always appreciably lower than the compressive strength. Consistent with the similar exponents for shear and compression in the strength-bone volume fraction relation, the ratio of shear to compressive strengths (**Figure 2-4**) did not depend on bone volume fraction (p=0.24) or anatomic site (p=0.13). However, this ratio did vary appreciably (mean±SD = 0.44±0.16; range=0.25–1.00) and was partially explained by microarchitecture (**Table 2-2**), most notably the intra-specimen standard deviation of trabecular separation (Tb.Sp.SD, R^2=0.23, p<0.005). For some specimens having low bone volume fraction (BV/TV<0.20), the ratio of shear to compressive strengths was close to the value of 0.58 as predicted by a traditional (assuming isotropy and strength symmetry) von Mises criterion, but at higher bone volume fraction the von Mises criterion over-predicted this ratio.

Analysis of the amount of yielded tissue at the apparent-level yield point revealed a number of differences in the underlying failure mechanisms. While the total proportion of yielded tissue was only slightly lower for shear than compression loading (**Figure 2-5**), there were much greater differences in the mode of tissue-level failure. For shear, there was predominantly tensile tissue-level yielding regardless of bone volume fraction, whereas for compression, there was tensile tissue-level yielding at low bone volume fraction and compressive tissue-level yielding otherwise (**Figure 2-6**). Visual inspection revealed that for shear loading, there was mainly tensile stretching of the obliquely oriented trabeculae regardless of bone volume fraction (**Figure 2-7**). This tensile yield pattern appeared to occur primarily along continuous load paths that were oriented at approximately 45^0 with respect to the main trabecular orientation. However, for compression loading, there was mainly tensile failure of horizontal trabeculae for specimens with low bone volume fraction and otherwise mainly compressive failure of longitudinal trabeculae (**Figure 2-7**). This tensile failure of the horizontal trabeculae was the result of kinematic large deformation-related bending of the vertical trabeculae: when neighboring vertical trabeculae bent away from each other in opposite directions, the interconnecting horizontal trabeculae were stretched.

For the sub-study on torsion behavior, we found that the torsion strength varied in a power law fashion with bone volume fraction (**Figure 2-3**, R^2=0.96). The constant in the power law regression for torsional strength was significantly different from the constant of the regression of shear strength ($p<0.001$), but the exponents were not different ($p=0.25$, Tukey HSD test). After adjusting for bone volume fraction, general linear regression modeling indicated that the ratio of mean torsional strength to mean shear strength was 0.57, confirming that the apparent-level yield strength of trabecular bone is much lower under torsional loading relative to pure shear loading. Likewise, the ratio of the adjusted mean for torsion strength to compression strength was 0.24.

2.4. Discussion

These results show that human trabecular bone is generally much weaker in shear than compression at the apparent level, reflecting different failure mechanisms at the tissue level. Although the ratio of shear to compressive strengths did not depend on bone volume fraction, it did depend on the trabecular microarchitecture, particularly at low bone volume fraction for which the compressive and shear strengths were almost equal for some specimens. This dependence reflected a change in tissue-level failure mechanism for compressive loading as bone volume fraction decreases whereby kinematic large-deformation effects become important [47, 56] as adjacent vertical trabeculae bend apart from each other and stretch the connecting horizontal trabeculae. There was not any such dependence of the failure mechanism on bone volume fraction for shear loading. Thus, for some specimens with low bone volume fraction, depending on the micro-architecture, the compressive strength could fall low enough to approach the shear strength.

At the tissue level, one novel finding was the dominance of tensile yield of obliquely oriented trabeculae for pure shear loading. Because of the difficulty of probing

failure mechanisms using purely experimental models, most previous studies on pure shear [39, 42, 57] loading have described only apparent-level strength properties and have been unable to directly address tissue-level failure mechanisms. In general, pure shear loading along the main trabecular orientation, as simulated in our study, is equivalent to compression-tension biaxial loading at 45^0 to the main trabecular orientation. This equivalence is reflected in the observed failure pattern (**Figure 2-7**, left panels) of predominantly tensile yield due to stretching of the trabeculae oriented along the principal tensile stress direction at an angle of 45^0 with respect to main trabecular orientation. There is only a minor degree of compressive yield along the (perpendicular) principal compressive stress direction because the tissue is weaker in tension than compression, and thus yielding will occur preferentially for tensile loading even if tissue-level tensile and compressive stresses are equal. Interestingly, these failure mechanisms appear to be different than those for uniaxial apparent-level 45^0 off-axis loading. For example, our earlier work [18] showed that uniaxial compression of human trabecular bone caused predominantly tissue-level tensile yielding due to bending of individual trabeculae (again, which fail primarily in tension because the tissue is so weak in tension). It is not clear how a superimposed apparent-level tensile loading perpendicular to such 45^0 off-axis uniaxial compressive loading would alter such failure mechanisms and study of such bi-axial failure mechanisms remains a topic for future research. Previously, we also proposed that torsion of bovine tibial trabecular bone causes failure via appreciable bending of individual trabeculae [19]. Although torsion and shear loading both produce shear stresses in the specimen at the apparent level, those torsion results cannot be directly compared to those from our pure shear simulations because shear stresses across the specimen are not uniform in a pure torsion test and for trabecular bone this may cause different tissue-level failure mechanisms.

These observations on tissue-level failure mechanisms constitute computer-generated predictions and therefore await direct experimental validation. In the meanwhile, microdamage in trabecular bone induced from mechanical testing has been correlated with the structure model index [58, 59]. Consistent with that finding, we found that the total amount (proportion) of yielded tissue was also significantly correlated to SMI (**Table 2-2**). For specimens with low bone volume fraction loaded under compression, we found that failure occurred mostly in the horizontal trabeculae. This is consistent with the findings from experiments on human vertebral bone [60] in which it was observed that complete fracture of trabeculae was confined to the horizontal trabeculae—presumably fracture of individual trabeculae only occurs when trabecular are excessively stretched primarily uniaxially. Finite element studies by other investigators have also shown good agreement between predicted distributions of tissue-level stress and directly imaged histological sections of microdamage [61, 62].

At the apparent level, we found an influence of intra-specimen heterogeneity in trabecular microarchitecture on the ratio of shear to compressive strengths. Interestingly, this intra-specimen variation contributed more to a decrease in compressive strength of low volume fraction specimens than to any effect on the shear strength (**Table 2-2**). Similarly, the negative correlation between the degree of anisotropy (DA) and the shear to-compressive strength ratio implies that a more anisotropic structure renders the bone

equally susceptible to shear or compressive failure, more so due to the decrease in compressive strength than any effect on shear strength. Other investigators have reported similar observations, in which an increase in intra-specimen variability of microarchitecture of vertebral bone decreased stiffness [63] [64] [65] and strength [63] under compression. Similarly, it has been proposed that heightened trabecular anisotropy might render the proximal femur more susceptible to fracture [45]. Our results suggest that these intra-specimen heterogeneity effects primarily degrade the compressive strength and have less influence on the shear strength.

The validity of our computational results for apparent-level strength is supported by results from various previous experiments. Our compressive strength results were directly validated by our own experiments, and the exponent of about 1.7 in our strength-bone volume relation is consistent with reported power law relations from various other compression experiments, which are in range 1.5–2.0 [14, 31]. Since many experimental studies have studied shear failure by testing cylindrical cores of trabecular bone in torsion [26, 35, 39, 41], to help interpret that body of work we performed the sub-study to directly compare apparent-level yield strength derived from torsion vs. pure shear loading. That study found statistically similar exponents in the yield strength-bone volume fraction relation for the two loading modes, but much lower strength for torsion than pure shear (ratio of mean strengths=0.57 for n=15 specimens). This ratio is close to the value of 0.61 obtained for the ratio of mean torsion to shear ultimate strengths as measured experimentally for human femoral bone [39]. Similarly, the ratio of mean torsion strength to mean compression strength for these 15 specimens was 0.24, which is in close agreement with the value of 0.22 obtained in a much larger experiment on human trabecular bone [26]. Further, after accounting for variations in bone volume fraction, average values of torsional yield strength from our simulations agreed well in an absolute sense with the literature data from multiple experiments (**Figure 2-8**). Finally, a recent experiment on human trabecular bone reported statistically similar exponents for the strength-density relation for compression vs. torsion [26], just as we did (1.74 vs. 1.85, p=0.25, see **Figure 2-3**).

Our study has a number of limitations. Although our models were well validated for compressive yield strength, we relied on computational models to extrapolate from compressive strength to shear strength. In general, the models had sufficiently high spatial resolution for numerical convergence but did not include such micro-scale features as intra-specimen variations in mineral density or tissue material properties, anisotropy of the bone tissue, or the geometric detail of any resorption spaces. While inclusion of such features can affect overall behavior [66] [67] [68, 69], their exclusion is unlikely to appreciably alter the relation between compression vs. shear yield strengths, which was our main focus. Even so, it is possible that more complex tissue-level material behavior, such as anisotropy in tissue yielding and postyield hardening [70, 71], or mechanical effects of micro-damage or micro-fracture, might lead to different tissue-level failure mechanisms, particularly in the post yield region of the apparent-level stress–strain curve. Further, particularly for specimens having low volume fraction, the apparent- level properties as estimated by these finite element models may be sensitive to the applied boundary condition [72, 73], which may introduce some error in these

estimates compared to the in vivo behavior. Finally, we only explored shear behavior in the axial-transverse plane and the shear failure behavior may differ for other planes some of which have been investigated in Chapter 4. Despite these limitations, these new results should provide an improved basis for assessing the role of shear failure of trabecular bone in structural analyses of whole bones and bone-implant systems.

Table 2-1: Specimen details for the final cohort (mean ± SD)

Anatomic Site	No. of Specimens [†] (male/female)	Age (years)	Bone Volume Fraction
Femoral Neck	25 (12/13)	70 ± 10	0.25 ± 0.07
Greater Trochanter	4 (4/0)	67 ± 12	0.11 ± 0.04
Proximal Tibia	8 (8/0)	64 ± 10	0.12 ± 0.04
Vertebral body	17 (12/5)	66 ± 8	0.09 ± 0.03
Pooled	54 (36/18)	68 ± 10	0.17 ± 0.09

Table 2-2: Pearson correlation coefficients for yield strength, shear-to-compression yield strength ratio, and the proportion of yielded tissue, all versus bone volume fraction (BV/TV) and various architecture parameters (n=39). Data are shown stratified by bone volume fraction (Pooled, n=39; Low, BV/TV < 0.20, n=23; High, BV/TV > 0.20, n=16). Italicized values have $p < 0.05$ at least.

	Yield Strength						Shear-to-Compression Strength Ratio			Proportion of Yielded Tissue (%)					
	Shear			Comp						Shear			Comp		
	Pooled	Low	High	Pooled	Low	High	Pooled	Low	High	Pooled	Low	High	Pooled	Low	High
BV/TV	*0.97*	*0.90*	*0.90*	*0.97*	*0.91*	*0.96*	-0.24	-0.22	-0.27	*0.62*	0.25	*0.54*	*0.55*	0.11	*0.67*
Conn-Den	*0.39*	*0.42*	-0.35	*0.37*	0.38	-0.35	-0.16	-0.19	0.04	0.15	-0.29	-0.05	0.09	-0.31	-0.05
SMI	*-0.84*	-0.38	*-0.79*	*-0.88*	*-0.64*	*-0.82*	0.32	0.36	0.19	*-0.56*	-0.25	-0.36	*-0.53*	-0.31	-0.43
Tb.N	*0.73*	*0.55*	0.21	*0.73*	*0.64*	0.15	-0.29	-0.36	0.04	*0.45*	-0.15	0.48	*0.39*	-0.06	0.39
Tb.Th	*0.86*	*0.71*	*0.61*	*0.88*	*0.67*	*0.72*	-0.22	-0.12	-0.32	*0.40*	-0.04	0.09	*0.40*	-0.05	0.30
Tb.Sp	*-0.69*	*-0.52*	-0.23	*-0.70*	*-0.65*	-0.16	*0.40*	*0.48*	-0.07	*-0.39*	0.13	*-0.51*	*-0.39*	-0.07	-0.41
Tb.(1/N).SD	*-0.36*	0.07	-0.29	*-0.41*	-0.21	-0.17	*0.43*	*0.53*	-0.14	-0.29	0.17	*-0.61*	*-0.42*	-0.26	-0.44
Tb.Th.SD	*0.59*	*0.77*	0.06	*0.62*	*0.65*	0.24	-0.16	0.03	-0.34	0.18	0.05	-0.26	0.22	-0.05	0.02
Tb.Sp.SD	*-0.53*	*-0.01*	-0.45	*-0.58*	-0.32	-0.37	*0.48*	*0.56*	-0.01	*-0.34*	0.16	*-0.62*	*-0.47*	-0.29	*-0.50*
DA	0.19	0.40	0.13	0.3	*0.71*	0.31	*-0.41*	*-0.43*	-0.25	0.14	0.18	0.03	*0.36*	*0.47*	0.26

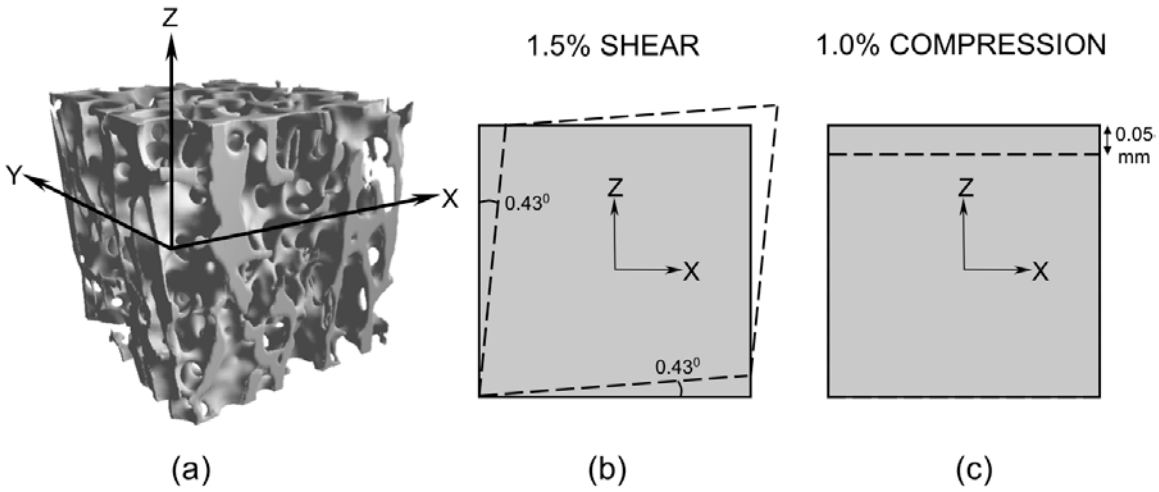

Figure 2-1: *(a)* A 5mm cube trabecular bone specimen with its Z-axis oriented along the main material orientation (the X-axis was selected randomly in the transverse plane) *(b)* An engineering XZ shear strain of 1.5% was applied for shear strength analysis, the dashed lines denoting the prescribed displacement boundary condition on four faces, the other two faces remaining unconstrained *(c)* A compressive normal strain of 1.0% was applied for compressive strength analysis, the dashed lines denoting the prescribed displacement boundary condition on the top face, the bottom face minimally fixed on rollers and the sides faces unconstrained.

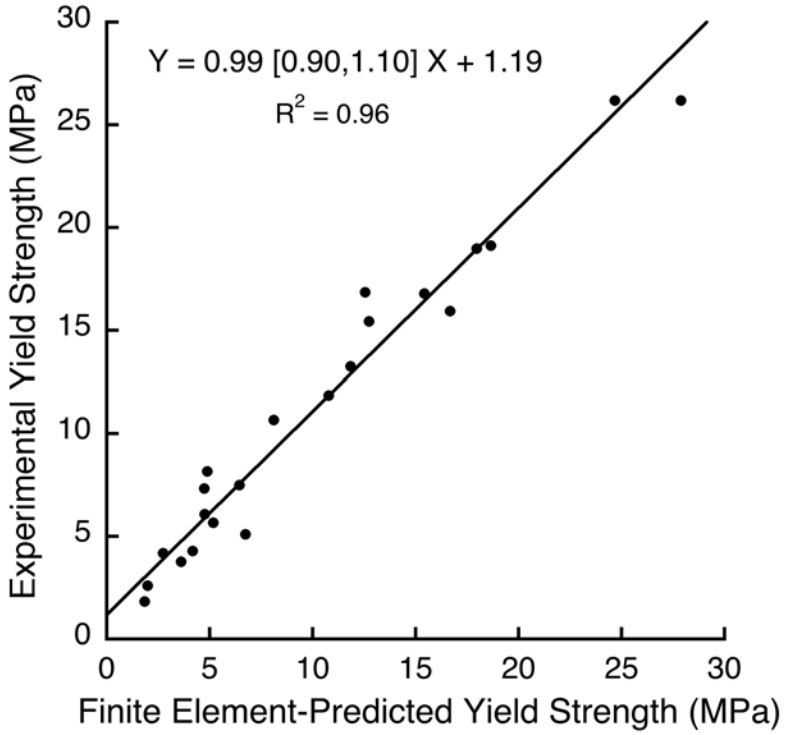

Figure 2-2: Validation of predictions of compressive yield strength, for the 22 specimens in this study that had both micro-CT scans and experimental measures of compressive yield strength. The same tissue-level effective modulus of 18.0 GPa was used in all models. Orthogonal regression was used since there were measurement errors in both experimental and finite element strength measures. Values in brackets represent the 95% confidence interval for the slope.

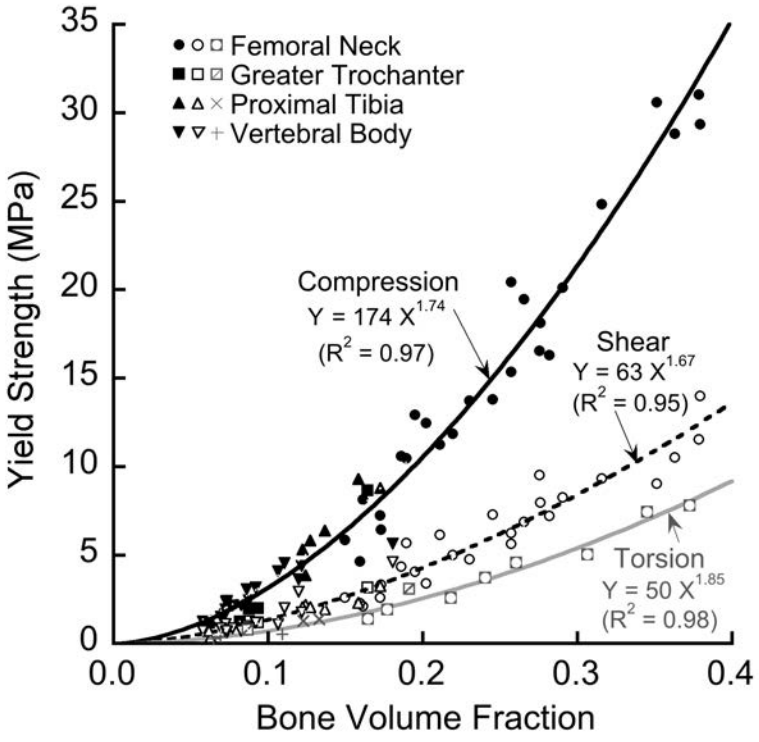

Figure 2-3: Variation of compressive (solid line), shear (dashed line), and torsion (light line) apparent-level 0.2% offset yield strengths with bone volume fraction.

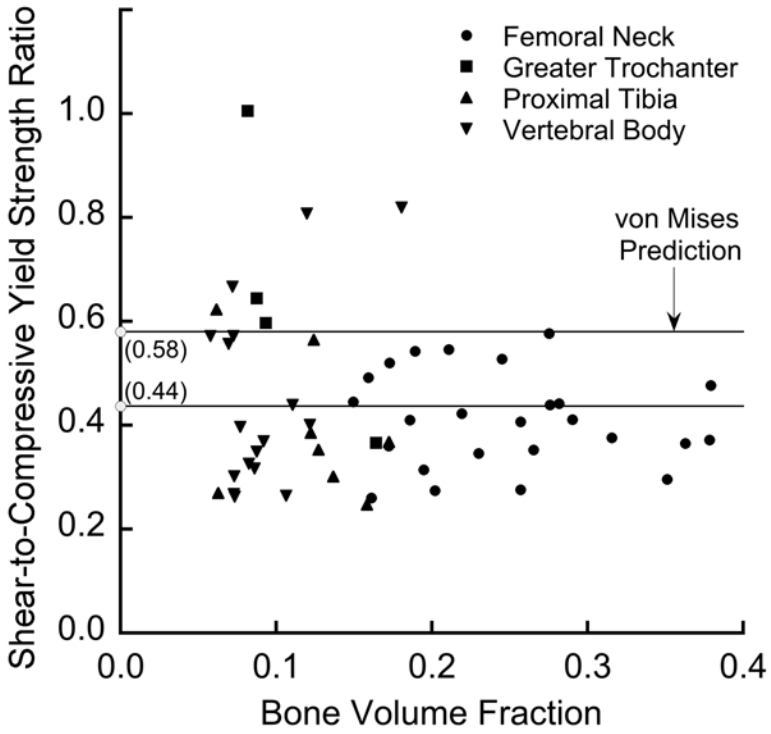

Figure 2-4: Variation of the ratio of shear to compressive yield strengths with the bone volume fraction. This ratio (mean ± SD = 0.44 ± 0.16 for 54 specimens) displayed additional scatter below a bone volume fraction of about 0.20. This ratio for the traditional von Mises criterion is 0.58.

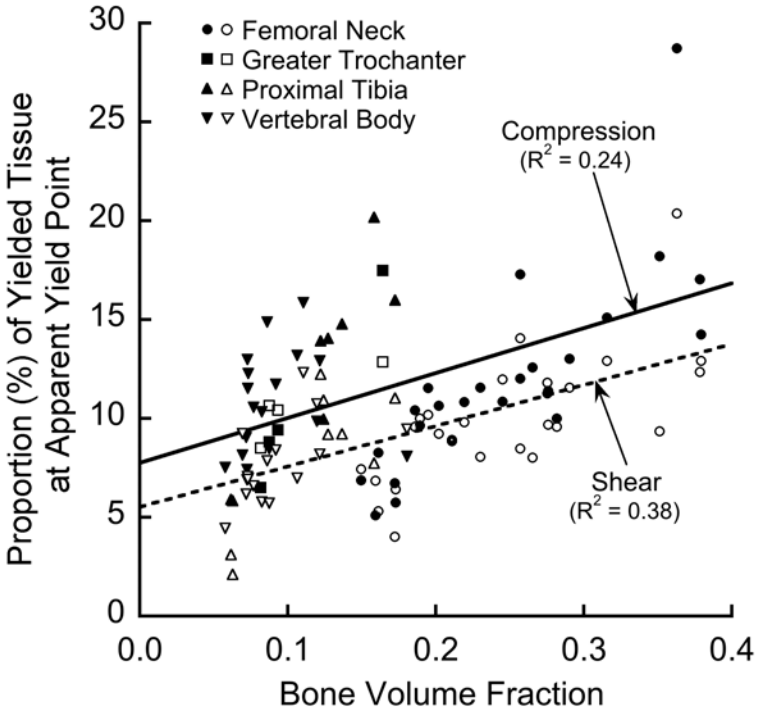

Figure 2-5: Variation of the proportion of yielded tissue (expressed as a percentage of total tissue in the bone specimen) at the apparent-level 0.2% offset yield point for shear and compression loading.

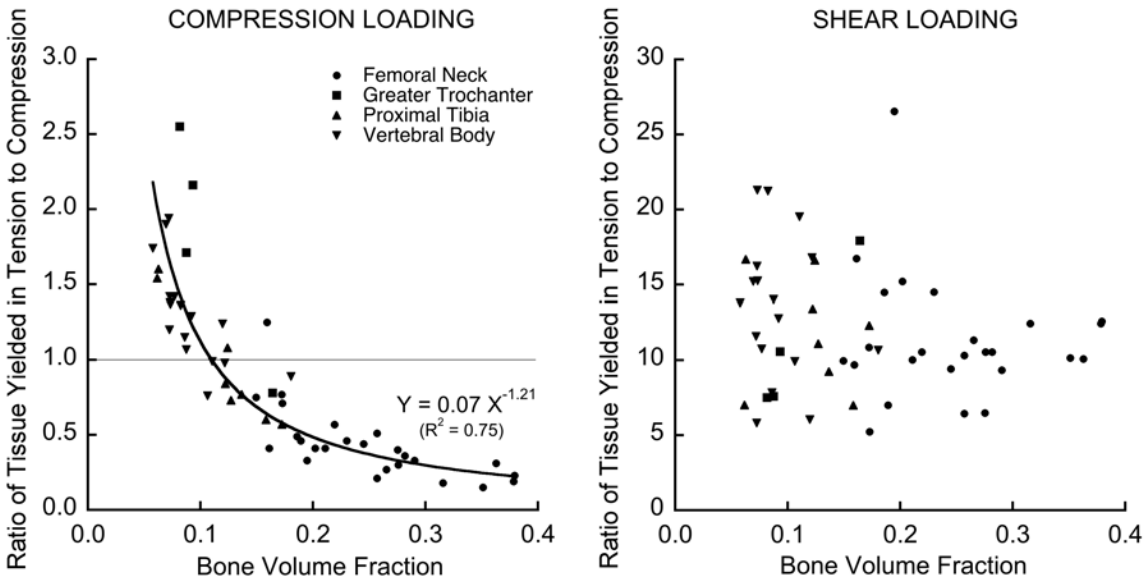

Figure 2-6: Variation of the ratio of tissue yielded in tension to tissue yielded in compression at the apparent-level 0.2% offset yield point, for compression (left) and shear (right) loading. Note the 10-fold difference in the vertical scales between plots.

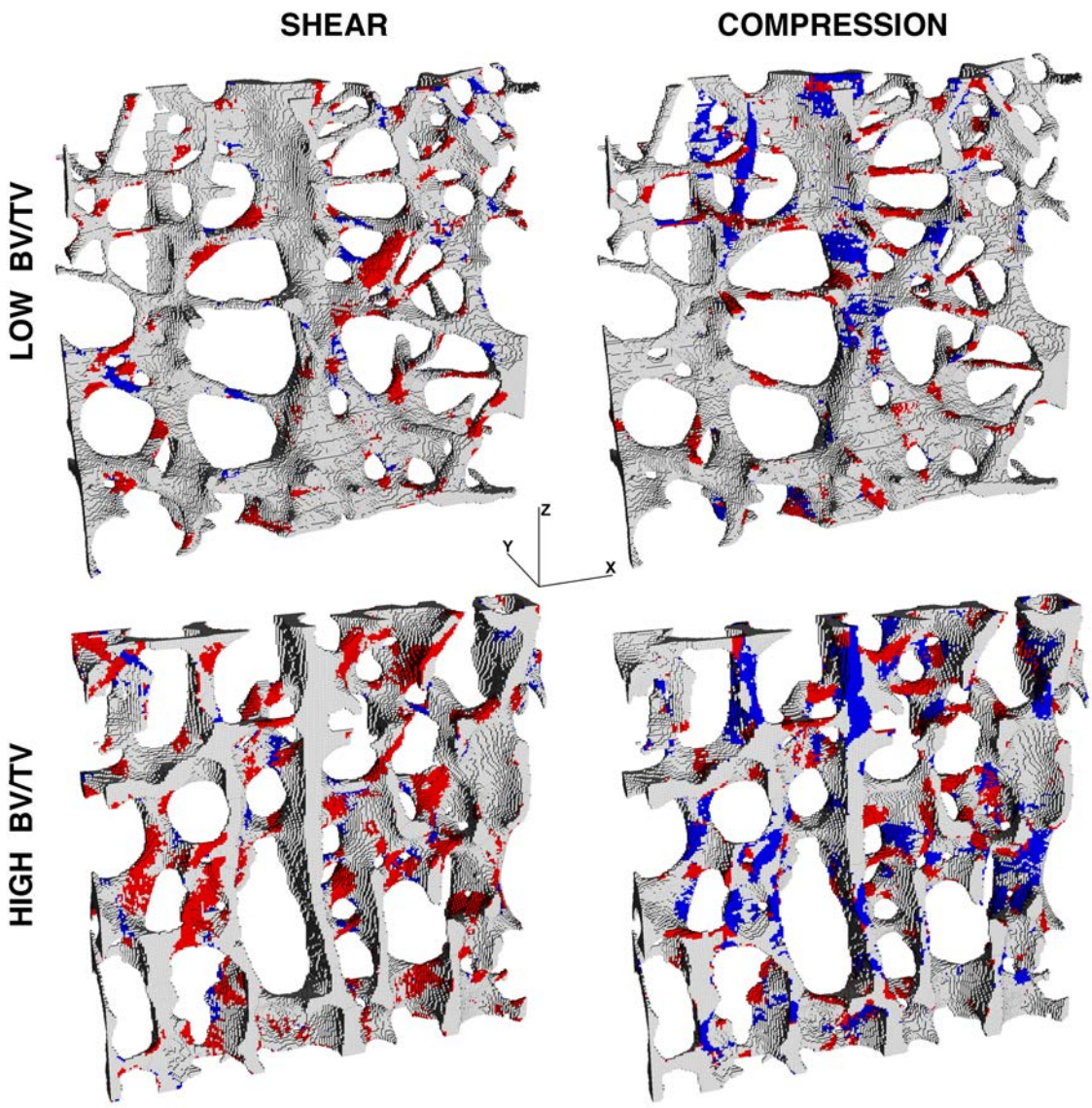

Figure 2-7: Distribution of tissue-level yielding for a thin slice for two specimens, of low (BV/TV = 0.07) and high (BV/TV = 0.26) bone volume fraction. Red regions denote tissue-level yield in tension and blue regions denote tissue-level yield in compression. The Z-axis denotes the main trabecular orientation.

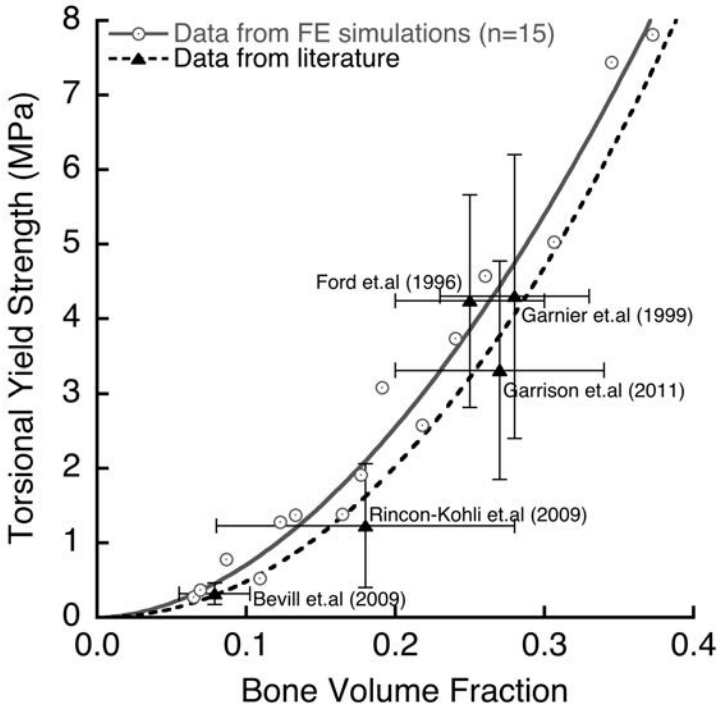

Figure 2-8: Literature comparison [26, 35, 39, 44] of torsional yield strength vs. bone volume fraction, for 15 specimens from this study. The error bars show one standard deviation around the mean value of bone volume fraction and yield strength. For studies that did not report apparent density, the bone volume fraction was calculated assuming a tissue density of 2.0 g/cm^3. The data from [73] is unpublished (n=6 vertebral body specimens).

3. BIAXIAL STRENGTH BEHAVIOR OF HUMAN TRABECULAR BONE

3.1. Introduction

During both habitual and traumatic loading, trabecular bone is often subjected to biaxial loads i.e. loads acting simultaneously along and transverse to the principal trabecular orientation. During gait loading, as a result of the direct action of the obliquely oriented compressive joint contact force and the associated bending of the femoral neck, the longitudinal trabeculae all the way from the femoral head to the medial femoral cortex are loaded primarily in compression whereas the corresponding transverse trabeculae in this region are loaded primarily in tension [74]. A similar biaxial loading pattern is also observed during a fall to the side on the greater trochanter, but with the tension-compression patterns reversed [75]. The biaxial strength behavior of trabecular bone is therefore potentially relevant to both bone adaptation under habitual loading and to whole-bone failure under traumatic loading. Concerning the latter, due to the increased structural and mechanical anisotropy of osteoporotic trabecular bone [45, 46, 76, 77], it has been proposed that increased mechanical anisotropy may be an independent risk factor for hip fracture [78], although understanding of this issue remains incomplete.

Despite much previous research on the multiaxial behavior of bone, the biaxial failure characteristics of human trabecular bone remain unclear for bone having a low bone volume fraction, in which the degree of mechanical anisotropy can be high. A fabric-based, ellipsoidal, Tsai-Wu-type of failure criterion has been formulated for trabecular bone [21]. However, triaxial compression experiments on bovine tibial bone did not support the quadratic ellipsoidal shape of this criterion [22] and axial-torsion experiments have pointed instead to a cellular-solid-type criterion having a non-ellipsoidal shape [19]. Non-linear micro-CT based finite element simulations on bovine [23] and human [24] trabecular bone — all having high bone volume fraction — provided further evidence of the need for a multiaxial criterion that is not ellipsoidal in shape, due primarily to the different failure mechanisms associated with the different loading directions. More recently, experiments and finite element simulations were performed to fit a piecewise quadratic Hill's criterion [26] and a ellipsoidal Tsai-Wu failure criterion, all as a function of bone volume fraction and fabric-based morphological anisotropy [27]. However, since these experiments and simulations only included the minimum number of load cases for formulation of a quadratic criterion — and given the aforementioned evidence from the prior triaxial compression experiments on bovine tibial bone [22] — it still remains unclear if the full biaxial failure envelope is indeed ellipsoidal in nature or if some alternative description would be more appropriate. We therefore sought to extend this previous research by further exploring the biaxial yield stress behavior of human trabecular bone in the axial-transverse plane, in which we spanned a wide range of loading conditions and focused on accounting also for a wide range of bone volume fraction, mechanical anisotropy, and microarchitecture.

3.2. Methods

We analyzed 15 specimens of morphologically diverse, human trabecular bone (cadaver age=63±12, 48-79; 4 female, 10 male), taken from four anatomic sites: vertebral body (n=4), femoral neck (n=7), greater trochanter (n=2) and proximal tibia (n=2). These specimens were machined as 8-mm-diameter cylindrical cores along their principal material orientation and were scanned using micro-CT (Scanco Medical AG, Brüttisellen, Switzerland) at a voxel size of 10-22 microns. A 5-mm cube was virtually extracted from the central portion of these images and the trabecular microarchitecture parameters were calculated (Skyscan: CTAn software); the Euler angles of misalignment were also calculated by conducting six uniaxial linear elastic finite element analyses [52]. The angle of misalignment of each cube specimen was confirmed to be within $\pm 10^0$, ensuring the axes of the extracted cube specimens were adequately aligned with the principal material coordinate system.

Micro-CT images of the cube specimens, down-sampled to 20-22μm, were then used to generate finite element models by converting each cubic voxel into an 8-noded brick element. First, linear elastic analysis was performed on each specimen to calculate the elastic modulus in the longitudinal (E_L) and the two transverse directions (E_{T1}, E_{T2}). The percentage deviation from transverse isotropy (%DEV = $100(E_{T1}-E_{T2})/E_{T1}$) was 11.1±7.7 % for the 15 specimens, which we considered an acceptable error in assuming transverse isotropy of the specimens. Thereafter, the transverse direction for mechanical loading was chosen randomly for further analysis and the elastic anisotropy (EA) was defined as the ratio of the uniaxial moduli in the two directions ($EA = E_L/E_T$).

For all models, all finite elements were assigned the same hard-tissue material properties having an isotropic elastic modulus of 18.0 GPa, a Poisson's ratio of 0.3, and a rate-independent non-linear constitutive model with both elastic-plastic material and geometric kinematic non-linearities [53]. In the constitutive model, tissue-level failure was defined using a von-Mises yield criterion modified by a pseudo kinematic hardening parameter to account for the tension-compression strength asymmetry of the bone tissue. The tissue-level yield strains of 0.33% in tension and -0.81% in compression were chosen based on a prior calibration study [47]. This particular implementation has been shown to produce excellent agreement (R^2=0.96) with experimental results from uniaxial tests [47, 79].

For each cube specimen, 18-20 separate analyses were performed, each analysis representing a uniaxial or biaxial loading state. For the uniaxial simulations, an unconstrained roller displacement boundary condition was applied in the longitudinal or transverse direction, producing an apparent-level state of uniaxial stress. For the biaxial simulations, loading was defined using proportional loading in which each load path was uniquely defined by the ratio of the maximum applied strain in the longitudinal and transverse directions, the third direction left unconstrained, thereby producing a biaxial stress state in the principal material coordinate system. All analyses were performed using a highly scalable, implicit parallel finite element framework, Olympus [54] on a

Sun Constellation Linux Cluster (Ranger; Texas Advanced Computing Center, TX, USA), for a total of 275 non-linear analyses requiring around 50,000 CPU hours.

The main outcome of these analyses was the apparent-level yield strength in the longitudinal and transverse directions, and calculated from that, the biaxial yield point. For uniaxial loading case, strain offset of 0.2% on the stress-strain curve in the loading direction was used to define the apparent-level yield point and the percentage tissue yielded was calculated at the apparent-level yield point, as done elsewhere [79]. Correlations were calculated for uniaxial yield strength and yield strains with bone volume fraction, elastic anisotropy and microarchitecture (**Table 3-1**) and regression equations were developed for the uniaxial yield strengths as a function of (when statistically significant) bone volume fraction, elastic anisotropy and/or microarchitecture (**Table 3-2**). For each biaxial loading case, the individual stress-strain curves in the longitudinal and transverse directions were used to define the longitudinal and transverse yield points, respectively, using a 0.2% strain offset criterion on each curve. A single biaxial yield point (referred subsequently as the "chronological" yield point) was then defined by the biaxial stress state at the instant of first yielding in either the longitudinal or transverse direction (**Figure 3-1**), as described elsewhere [19, 24]. In this way, biaxial failure was defined as the first instant of failure in either the longitudinal or transverse loading directions. The percentage tissue yielded was calculated at the chronological biaxial yield point for each loading case.

A further analysis of the yield points was conducted to develop a mathematical description of the biaxial yield envelope expressed as a function of bone volume fraction, elastic anisotropy, and microarchitecture. This analysis involved two steps. First, for all 18–20 load cases for each specimen, we plotted both the finite element-computed yield points associated with each of the longitudinal and transverse loading directions, in the biaxial stress space, and fit a separate curve to the yield points associated with failure in each of the two loading directions. This analysis showed that a quadratic ellipse [80] worked well for failure associated with each loading direction (**Figure 3-2**). The overall biaxial failure envelope was then taken as the inner surface created by each pair of longitudinal and transverse ellipses. For each specimen, the percentage error between the resulting fitted biaxial yield surface and the direct finite element-computed biaxial yield points was calculated using the difference of the vector norm of the biaxial stress from the origin [24], as follows,

$$\frac{\left\| \underline{\sigma}_{predicted} - \underline{\sigma}_{FE} \right\|}{\left\| \underline{\sigma}_{FE} \right\|} \times 100 \qquad \textit{(Equation 3-1)}$$

where $\underline{\sigma}_{predicted}$ is the predicted yield point from the fitted ellipses and $\underline{\sigma}_{FE}$ is the finite element-computed yield point. This error per simulated test was then averaged over all biaxial simulations for that individual specimen, and the resulting error per specimen was then averaged over all specimens in order to assess how well the fitted biaxial failure criterion represented the direct finite element-generated biaxial failure points. Second, to express the biaxial failure criterion as a function of bone volume fraction, elastic

anisotropy, and the various microarchitecture parameters, each resulting longitudinal and transverse ellipse for each individual specimen was then characterized by five coefficients: the diameter of the major and minor axes (a, b), the shift of the center from the origin (h, k) and an angle of tilt with the longitudinal axis (ϕ) (**Figure 3-2**); the equation of each ellipse given by the equation:

$$\left(\frac{\sigma_L^{'}}{a}\right)^2+\left(\frac{\sigma_T^{'}}{b}\right)^2=1 \qquad \begin{Bmatrix} \sigma_L^{'} \\ \sigma_T^{'} \end{Bmatrix}=\begin{bmatrix} \cos\phi & \sin\phi \\ -\sin\phi & \cos\phi \end{bmatrix}\begin{Bmatrix} \sigma_L-h \\ \sigma_T-k \end{Bmatrix} \qquad \textit{(Equation 3-2)}$$

where σ_L, σ_T are longitudinal and transverse stresses respectively. We then calculated pairwise correlations of the five coefficients of the fitted ellipse with bone volume fraction, elastic anisotropy, and the various microarchitecture parameters (**Table 3-1**).

We also developed a stress-normalized criterion. To do so, for each specimen, the finite element-computed longitudinal and transverse yield points, in each quadrant, were normalized by the respective uniaxial strengths for the specimen. For example, for a yield point in the longitudinal tension-transverse compression quadrant, all longitudinal strength values were divided by the uniaxial longitudinal tensile strength and all transverse strength values were divided by the transverse compressive strength of the specimen. A quadratic ellipse was then fit to these normalized longitudinal and transverse yield points (excluding the uniaxial points) and the five coefficients of each ellipse were calculated. Correlation analysis was then used to relate the five coefficients of the fitted normalized ellipses to bone volume fraction, elastic anisotropy, and the various microarchitecture parameters (**Table 3-1**). This was done for each individual specimen. Further, the normalized longitudinal and transverse yield points from all specimens were pooled together in a single plot and a quadratic ellipse was fit to each of the pooled normalized longitudinal and transverse yield points (referred subsequently as the "dual-ellipse" yield surface (**Figure 3-3**)). The percentage error was calculated between dual-ellipse yield surface and the pooled normalized longitudinal, transverse and chronological yield points using equation (3-1).

To facilitate comparison with the literature, two additional fits were performed on the pooled normalized chronological yield points (**Figure 3-4, Table 3-3**) – a single quadratic ellipse as described in equation (3-2) and a quartic super-ellipse similar to the modified super-ellipsoid equation from Bayraktar et. al [24]:

$$\left(\frac{\hat{\sigma}_L^{'}}{r_L}\right)^4+\left(\frac{\hat{\sigma}_T^{'}}{r_T}\right)^4+\left(\frac{t_L\hat{\sigma}_L^{'}+t_T\hat{\sigma}_T^{'}}{r_L+r_T}\right)^4=1 \quad \begin{Bmatrix} \hat{\sigma}_L^{'} \\ \hat{\sigma}_T^{'} \end{Bmatrix}=\begin{bmatrix} \cos\phi & \sin\phi \\ -\sin\phi & \cos\phi \end{bmatrix}\begin{Bmatrix} \hat{\sigma}_L-c_L \\ \hat{\sigma}_T-c_T \end{Bmatrix} \qquad \textit{(Equation 3-3)}$$

where $\hat{\sigma}_L$, $\hat{\sigma}_T$ are normalized longitudinal and transverse stresses respectively and c_L, c_T, t_L, t_T, r_L, r_T and ϕ are parameters of the equation. The percentage error (*equation 3-1*) between the finite element-computed normalized chronological yield points and the corresponding predictions from the dual–ellipse yield surface, single ellipse surface and

the quartic super-ellipse surface were calculated. To explore the sensitivity of biaxial yield strength on an alternate definition of yielding, we calculated the yield point based on a equivalent stress-strain curve as used in a recent study [27]. The equivalent yield data from all analyses were normalized with the respective uniaxial strengths of each specimen and the pooled data from all specimens were plotted in a single plot (Figure 5) and a single quadratic ellipse was fit to the pooled equivalent yield data and was compared with the dual-ellipse surface.

Finally, to gain insight into specific aspects of the biaxial failure behavior, the normalized dual-ellipse yield surface, coupled with its underlying regressions between uniaxial strength and bone volume fraction and elastic anisotropy, were used to calculate the variation of biaxial strength with elastic anisotropy for three constant values of bone volume fraction, all done for two relevant biaxial loading cases. The tissue-level yielding for these two biaxial compression-tension loading cases were investigated for three specimens from the proximal femur region (2 femoral neck, 1 greater trochanter).

3.3. Results

For each specimen, the yield surface in the biaxial stress space, as computed by the finite element analyses, was well represented by the combination of the longitudinal and transverse ellipses (**Figure 3-2**). Across all 15 specimens, the mean (± SD) error between the finite element-computed yield points for the longitudinal loading direction and the fitted longitudinal ellipse was 2.9 ± 0.7%; for the transverse loading direction the corresponding error was 3.3 ± 0.7%. As expected, the major and minor diameters of the ellipses (a,b) increased with increasing bone volume fraction (**Table 3-1**). We also found that minor diameters (b) decreased with increasing elastic anisotropy and therefore the aspect ratio (a/b) increased with elastic anisotropy. In addition, the angle of tilt (ϕ) of the ellipses decreased with increasing elastic anisotropy asymptotically tending to zero for highly anisotropic specimens. The elastic anisotropy was not correlated to the bone volume fraction ($p=0.20$) and was only weakly correlated to the morphological degree of anisotropy, DA ($r=0.50$, $p=0.06$).

For uniaxial loading cases, the yield strength under longitudinal loading was correlated to bone volume fraction but under transverse loading was correlated to both bone volume fraction and elastic anisotropy (**Table 3-1**). Statistical analysis revealed that power law regressions could well describe the variation in uniaxial strength when bone volume fraction and/or elastic anisotropy served as the independent variables; the microarchitecture did not provide any additional statistical association (**Table 3-2**). The yield strain for longitudinal compression increased with bone volume fraction ($r=0.80$, $p=0.0003$) but for transverse compression did not ($p=0.22$).

As a result of similar associations between uniaxial yield strengths and the various coefficients of the longitudinal and transverse yield ellipses, the coefficients of the normalized longitudinal and transverse yield ellipses depended only weakly on bone volume fraction, elastic anisotropy, or microarchitecture (**Table 3-1**). This weak dependence was also evident in the small amount of scatter in the normalized

longitudinal and transverse yield data pooled from all specimens (**Figure 3-3**), indicating that the residual variations in the biaxial strength were minor after accounting for the variations in uniaxial strength. This set of pooled normalized longitudinal and transverse yield data from all specimens was well described by a single dual-ellipse yield surface (**Figure 3-3**, **Table 3-3**), which had a mean (±SD) error of 3.9 ± 1.7% and 6.1 ± 2.5% for the fitted normalized longitudinal and transverse ellipses, respectively. The pooled normalized (chronological) yield points was best described by the dual-ellipse yield surface (**Figure 3-4a**, mean ± SD error = 4.8 ± 4.1%), followed by the quartic-super-ellipse yield surface (**Figure 3-4b**, mean ± SD error = 5.2 ± 4.2%) and then the single-ellipse yield surface (**Figure 3-4c**, mean ± SD error = 6.5 ± 4.6%). The point of intersection of the dual–ellipse yield surface was close to 1.0 for longitudinal tension and transverse tension, as expected, but was greater than 1.0 for longitudinal compression and transverse compression (1.04 and 1.11 for longitudinal compression and transverse compression respectively).

The pooled equivalent yield data was well described a quadratic ellipse with a mean (±SD) error of 4.9 ± 4.4% (**Figure 3-5**). However, the point of intersection of this ellipse was around 1.5 for transverse tension and compression loading thereby over-predicting the transverse uniaxial strengths. For a biaxial loading with high proportion of longitudinal loading, the equivalent yield points were close to the longitudinal ellipse. However, for a biaxial loading with high proportion of transverse loading, the equivalent yield points lay between the longitudinal and transverse yield ellipses (**Figure 3-5**).

The normalized dual-ellipse yield surface, coupled with the regressions on uniaxial strength, revealed that the biaxial yield strength for two biaxial compression-tension loading scenarios decreased with increasing elastic anisotropy, independent of the bone volume fraction (**Figure 3-6**). For a longitudinal compression and transverse tension biaxial loading having a ratio of ~5, the biaxial apparent yield point was determined by the transverse response for all three specimens. Visual inspection revealed that for this loading case, there was predominantly tensile failure of the horizontally oriented trabeculae (**Figure 3-7**) for all three specimens. Between the two femoral neck specimens with similar bone volume fraction, the more anisotropic specimen sustained only little tissue-level failure at the overall biaxial failure point. However, for longitudinal tension and transverse compression in a ratio of ~5, the direction determining the biaxial yield point depended on anisotropy. For example, for the highly anisotropic femoral neck specimen, the transverse direction yielded first whereas for the two less anisotropic specimens, the longitudinal direction yielded first. This is consistent with the observation that the biaxial failure, for this particular biaxial loading, transitions from the longitudinal to the transverse direction above an elastic anisotropy of around 6.0 (**Figure 3-6**). Visual inspection revealed that for this type of biaxial loading, there was predominantly tensile tissue failure for all specimens. This failure distribution was primarily distributed in the longitudinally oriented trabeculae for the less anisotropic specimens and equally distributed between the longitudinally and horizontally oriented trabeculae for the highly anisotropic specimen (**Figure 3-7**).

3.4. Discussion

The results of this computational analysis suggest that the biaxial yield behavior of human trabecular bone, in the axial-transverse plane, can be described well by a dual-ellipse surface, the size of which depends primarily on bone volume fraction, whereas the shape (i.e. aspect ratio) and orientation of which depend primarily on elastic anisotropy. This dependence of biaxial yield strength parameters on bone volume fraction and elastic anisotropy can be primarily attributed to a similar dependence of the uniaxial yield strengths which leads to relatively little unexplained inter-specimen variation of biaxial yield behavior after accounting for the uniaxial yield behavior. Using parametric study of this normalized failure criterion, expressed as a function of the bone volume fraction and elastic anisotropy, we found that, independent of bone volume fraction, an increase in the elastic anisotropy, which is primarily associated with a decrease in transverse strength, leads to a simultaneous increase in aspect ratio and decrease in orientation of the biaxial yield surface, which together reduce biaxial strength by making the specimen more susceptible to failure in the weaker transverse direction.

One advantage of performing such investigations using high-resolution, specimen-specific finite element simulation is that insight can be obtained into the underlying failure mechanisms, which would be difficult to achieve using just experimental techniques. For example, under a combined longitudinal-compression and transverse-tension biaxial loading, as might typically occur in the proximal femur during gait [74], we found that trabecular bone is likely to yield first due to failure associated with the transverse tensile loading component because of predominant failure at the tissue level of the horizontally oriented trabeculae via tensile failure (bone tissue is particularly weak in tension). However, for a combined longitudinal-tension and transverse-compression biaxial loading, that might typically occur in the proximal femur during a sideways fall [75] , the microstructurally weaker direction (transverse) is now loaded in the stronger tissue-failure mode (compression) and the microstructurally stronger direction (longitudinal) is loaded in the weaker tissue-failure mode (tension). Therefore, the apparent-level yield can occur either in the longitudinal or transverse direction, depending on the degree of mechanical anisotropy of the specimen. For a less anisotropic specimen, the apparent-level yield points in the longitudinal and transverse directions are similar but for a highly anisotropic specimen, we found that apparent-level yield occurs first in the transverse direction. Further, in a highly anisotropic specimen, since there are proportionately fewer and thinner horizontally oriented trabeculae [45, 81] [82], the trabecular microstructure can sustain only a small amount of tissue failure before overall apparent-level yield in the transverse direction. Therefore, in the context of osteoporosis, under the biaxial loading of the trabecular bone within the proximal femur that might typically occur during a sideways fall, for a given bone volume fracture, a specimen having increased mechanical anisotropy can be susceptible to premature yield in the non-primary loading direction. This mechanism might help explain results from previous studies showing that when matched for bone volume fracture, patients with hip fractures had a more anisotropic trabecular microstructure compared to non-fracture controls [45, 78].

The results from these biaxial simulations also lend insight into the yield behavior of human trabecular bone under off-axis compression loading. According to principles of stress transformation, a 45^0 off-axis compression at a stress σ is equivalent to a combination of on-axis longitudinal and transverse compression loading at $\sigma/2$ and shear loading at $\tau=\sigma/2$. The on-axis longitudinal compressive yield strains depend on bone volume fraction, but since transverse compressive yield strains do not depend on bone volume fraction and shear yield strains depend only weakly on bone volume fraction [79], taken together it helps explain why 45^0 off-axis compressive yield strains do not depend on bone volume fraction although on-axis longitudinal compressive yield strains do [18].

Our new results are consistent with previous studies that have defined the multi-axial failure envelope for trabecular bone as an intersection of multiple surfaces as opposed to just a single quadratic-type surface. Our yield envelope consisting of two intersecting ellipses in stress space is similar to what has been proposed previously for bovine bone in strain space, based on micro-CT-based finite element analysis [23]. Two intersecting ellipses has also been used to define a failure envelope for cellular solids [28] under biaxial loading, based on assumptions of plastic collapse of cell walls as the primary failure mode, while others also proposed two separate ellipsoidal envelopes based on a generalized Hill's failure criterion [25]. Alternatively, the inner surface of the two intersecting ellipses can be defined by a super-ellipsoid equation as done previously for human femoral bone in strain space [24]. The equation employed in the current study is similar in form to the modified super-ellipsoid equation [24], with exponents equated to four and an additional parameter introduced to quantify the angle of tilt. The angle of tilt is introduced since the biaxial yield was defined in stress space as opposed to strain space in the previous study [24]. While both strain- and stress-based criteria can be incorporated into computational models, we are reporting the criterion in stress space since a stress-based criterion facilitates direct comparison with multi-axial experiments because it is not necessary to measure any Poisson effects. We also observed that the angle of tilt of the yield ellipses varies with elastic anisotropy, which is consistent with previous studies on fiber-reinforced composite materials [83] that have suggested the angle of tilt as a function of anisotropy.

One prominent question concerning multi-axial behavior of human trabecular bone remains whether the yield behavior can be described by the quadratic Tsai-Wu criterion. A recent study [27], specifically addressing the failure behavior of human vertebral trabecular bone, used Cowin's [21] type of formulation to propose a single Tsai-Wu ellipsoidal criterion as a function of both bone volume fraction and fabric based anisotropy. However, that study fit data generated from finite element simulations using just a few loading cases and as such did not have a sufficient number of degrees of freedom to detect more complex behavior. In a previous study on tri-axial compressive behavior of bovine trabecular bone, it was found that although one can indeed fit a single Tsai-Wu quadratic yield envelope to triaxial data, the fit was not general and therefore did not work well for altered loading conditions [22]. Alternatively, as shown here, the yield surface could be well described by a quartic super-ellipse equation. That yield surface has box-like shape, which is also supported by theoretical and experimental

studies on open-cell foams [28, 84]. In the normalized stress space, we observed that the angle of tilt of the longitudinal ellipse is close to 90^0, which suggests that failure responses in the longitudinal direction occur around a constant principal stress. On the other hand, the transverse ellipse had an angle of tilt of 22^0, which, at around halfway 0^0 and 45^0, suggests that failure in the transverse direction is somewhere between a principal stress type failure and quadratic von-Mises type failure (the angle of tilt for a von-Mises yield equation = 45^0). These results taken together therefore suggest that the biaxial failure of human trabecular bone in the axial-transverse plane is not entirely quadratic. Studies on other porous materials like polymeric foams have used non-quadratic forms for yield function [85] which is well supported by experiments.

One unique challenge in comparing different multi-axial failure criteria across studies is to account for the failure in the multiple different loading directions. While in this study we chose to define the apparent–level yield point based on two individual stress–strain curves in the longitudinal and transverse directions as done previously in other studies [19, 23, 24], Wolfram et.al [27] defined the apparent-level yield point based on an "equivalent" stress-strain curve constructed from the components of the stress and strain tensor. Similarly, other studies on multi-axial behavior of cortical bone [86], cellular solids [87] and polymers [88] have used equivalent stress and/or strain definitions to define a composite-type yield point under multi-axial loading. Our results show that while the equivalent approach works well for a biaxial loading having a high proportion of longitudinal loading, such biaxial yield points are overestimated when there is substantial transverse loading (**Figure 3-5**). This is reflected in a 50% over-prediction of the uniaxial transverse yield strengths from the elliptical fit to the equivalent yield points (Figure 5). Using the chronological yield definition leads to only a minor over-prediction of uniaxial compressive yield strengths which can be attributed to edge effects of discrete trabeculae on the boundary [89]. Under predominantly longitudinal loading, the transverse stress is negligible due to the anisotropic nature of trabecular bone and therefore the biaxial equivalent stress-strain response closely resembles the uniaxial longitudinal stress-strain response. However, under a more predominantly transverse type of biaxial loading, the magnitude of transverse stress becomes comparable to the magnitude of longitudinal stress, and therefore the equivalent yield point lies somewhere between the yield points obtained from the longitudinal and transverse directions individually. The use of two separate stress-strain responses, one for each principal material direction, is more mechanistic in nature and allows one to interpret the mode of apparent-level yield in either the longitudinal or transverse trabecular orientation.

While we assumed trabecular bone to behave as a transversely isotropic material as assumed in previous studies [22, 27], its behavior is truly orthotropic [90]. The large scatter and error observed in elliptical fit in the transverse direction can be possibly explained by the random choice of the transverse direction. If we assume a significant difference in the elastic moduli in the two transverse directions, the observed scatter in the normalized chronological yield data can vary depending on the choice of the transverse plane, which may lead to higher or lower error estimates of the proposed dual-ellipse yield surface. It would be worthwhile to further explore the yield behavior in other

planes and include other loadings such as shear loading to get a complete picture of the yield behavior.

Our study has some limitations. First, at the tissue level we considered only plastic yielding as the failure mechanism under all biaxial loading modes. Based on cellular solid theory, different failure mechanisms such as brittle cracking under tension or elastic buckling under compression can lead to different failure envelopes under biaxial loading [28, 91]. While our elastic-plastic constitutive model was shown to give good agreement for both apparent-level and tissue-level yield for longitudinal compression loading (refer *Chapter 2*), there remains a need to investigate more sophisticated tissue-level constitutive models in these types of multi-axial computational studies since bone tissue material properties may change with age and disease [92, 93]. Second, we considered the bone tissue to be homogeneous and isotropic. The anisotropy of the bone tissue (i.e. material anisotropy) likely only has a small influence on the overall anisotropy of trabecular bone at the apparent level since the apparent level anisotropy is primarily due to the trabecular structure [7, 94, 95] (i.e. structural anisotropy). Likewise, the effects of mineral heterogeneity on the apparent behavior should be also minor [67, 96]. Third, we used displacement boundary conditions for generating the biaxial stress states in our finite element simulations. This may provide an upper bound on the effective biaxial strength whereas use of force boundary condition may provide a lower bound on the effective biaxial strength [97]. However, the effect of bone volume fraction and anisotropy should still reflect on the size, shape, and orientation of the yield ellipses irrespective of the boundary condition used.

Table 3-1: Correlation coefficients for the five ellipse parameters for each of the longitudinal and transverse yield ellipses, the four uniaxial strengths and the five ellipse parameters for each of the normalized longitudinal and transverse yield ellipses, with bone volume fraction (BV/TV), elastic anisotropy (EA), and a variety of microarchitecture parameters, for the n=15 specimens analyzed. Bold values have $p < 0.05$.

Variable	Biaxial Yield Strength										Uniaxial Yield Strength				Normalized Biaxial Yield Strength									
	Longitudinal Ellipse					Transverse Ellipse					Longitudinal		Transverse		Longitudinal Ellipse					Transverse Ellipse				
	a	b	h	k	ϕ	a	b	h	k	ϕ	Tens	Comp	Tens	Comp	a	b	h	k	ϕ	a	b	h	k	ϕ
BV/TV	**0.99**	**0.96**	**-0.99**	**-0.91**	0.40	**0.99**	**0.91**	**-0.98**	**-0.89**	**0.59**	**0.99**	**0.99**	**0.91**	**0.90**	-0.32	**-0.71**	**0.77**	0.01	**0.56**	-0.47	**-0.56**	0.22	0.20	0.40
EA	-0.37	**-0.55**	0.36	**0.59**	**-0.78**	-0.33	**-0.61**	0.49	**0.60**	**-0.68**	-0.34	-0.37	**-0.62**	**-0.61**	**0.82**	0.29	-0.45	-0.15	**-0.67**	0.19	**0.56**	0.27	**-0.61**	0.10
SMI	**-0.90**	**-0.86**	**0.89**	**0.82**	-0.45	**-0.88**	**-0.83**	**0.88**	**0.82**	**-0.64**	**-0.90**	**-0.90**	**-0.83**	**-0.82**	0.40	**0.63**	**-0.72**	-0.06	**-0.62**	**0.57**	**0.56**	-0.30	-0.08	**-0.56**
Tb.Th	**0.87**	**0.77**	**-0.88**	**-0.69**	0.02	**0.89**	**0.67**	**-0.82**	**-0.66**	0.24	**0.88**	**0.87**	**0.68**	**0.66**	-0.01	**-0.60**	**0.58**	-0.21	0.22	-0.27	-0.39	0.12	0.05	0.28
Tb.N	**0.94**	**0.92**	**-0.94**	**-0.89**	0.51	**0.93**	**0.89**	**-0.93**	**-0.88**	**0.69**	**0.94**	**0.94**	**0.90**	**0.89**	-0.42	**-0.70**	**0.78**	0.09	**0.66**	**-0.55**	**-0.59**	0.26	0.19	0.47
Tb.Sp	**-0.84**	**-0.77**	**0.84**	**0.71**	-0.42	**-0.84**	**-0.72**	**0.80**	**0.70**	**-0.59**	**-0.84**	**-0.84**	**-0.73**	**-0.72**	0.34	**0.76**	**-0.87**	-0.20	**-0.55**	**0.58**	**0.58**	-0.50	-0.14	**-0.54**
DA	0.36	0.16	-0.35	-0.05	-0.40	0.37	0.08	-0.25	-0.05	-0.15	0.39	0.35	0.10	0.07	0.26	-0.09	0.10	-0.31	-0.09	-0.39	-0.07	0.05	-0.41	0.37
Conn-Dens.	**0.73**	**0.70**	**-0.72**	**-0.68**	0.43	**0.71**	**0.68**	**-0.72**	**-0.67**	**0.56**	**0.72**	**0.72**	**0.68**	**0.67**	-0.37	**-0.56**	**0.64**	0.31	0.51	-0.49	**-0.52**	0.19	0.36	0.25
Tb.Th.SD	**0.71**	**0.56**	**-0.72**	-0.47	-0.22	**0.74**	0.44	**-0.64**	-0.42	0.02	**0.71**	**0.70**	0.42	0.40	0.17	**-0.62**	0.51	-0.25	-0.01	-0.23	-0.34	0.24	-0.11	0.29
Tb.Sp. SD	**-0.66**	**-0.60**	**0.66**	**0.53**	-0.37	**-0.65**	**-0.55**	**0.62**	**0.53**	-0.50	**-0.66**	**-0.65**	**-0.57**	**-0.55**	0.34	**0.69**	**-0.82**	-0.31	-0.46	**0.62**	**0.54**	**-0.62**	-0.10	**-0.53**

DA=Degree of Anisotropy, SMI=Structure Model Index, Tb.Th=Trabecular Thickness, Tb.N=Trabecular Number, Tb.Sp=Trabecular Separation, Conn-Dens.=Connectivity Density, Tb.Th.SD=Standard Deviation of Trabecular Thickness, Tb.Sp.SD=Standard Deviation of Trabecular Separation

Table 3-2: Power law regressions relating the four uniaxial yield strengths with bone volume fraction (BV/TV) and elastic anisotropy (EA) for n=15 specimens analyzed. ($p<0.001$ for all regressions)

	$c\,(BV/TV)^{m1}(EA)^{m2}$			
	c	m1	m2	R^2
Longitudinal Tension (σ_{LT}^{y})	81.2	1.53	0	0.99
Longitudinal Compression (σ_{LC}^{y})	183	1.73	0	0.99
Transverse Tension (σ_{TT}^{y})	76.3	1.33	-1.07	0.99
Transverse Compression (σ_{TC}^{y})	164	1.41	-1.30	0.99

Table 3-3: Coefficients of the single ellipse (*equation 3-2*), dual-ellipse and quartic super-ellipse fits (*equation 3-3*) to the pooled normalized chronological yield strength data

	a	b	h	k	ϕ
Single Ellipse	2.70	2.08	0.0220	-0.0496	40.6
Dual Ellipse					
Longitudinal	5.94	2.04	-0.0065	0.1019	84.9
Transverse	3.19	2.03	0.1381	-0.0233	21.6

	c_L	c_T	r_L	r_T	t_L	t_T	ϕ
Quartic SuperEllipse	0.0014	-0.0547	1.05	1.42	0.84	1.98	102.9

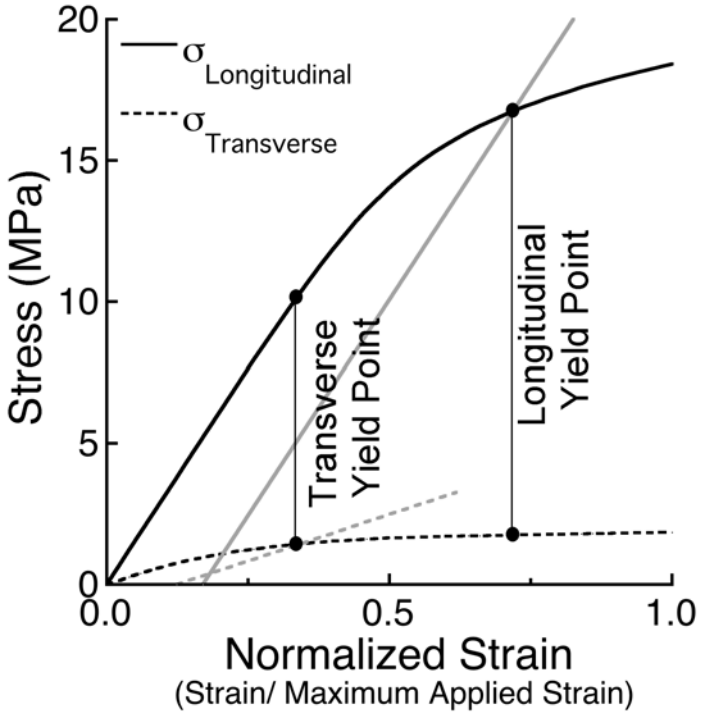

Figure 3-1: Definition of the chronological yield point. This graph depicts the stress-normalized strain responses in the longitudinal (solid line) and transverse (dotted line) directions for a single specimen loaded biaxially in the longitudinal and transverse directions. The normalized strains occur at the same instant in time for both responses. For this specimen, the ratio of maximum strain for the longitudinal to transverse directions was 0.73, and yielding first occurred along the transverse direction, which defined the chronological yield point.

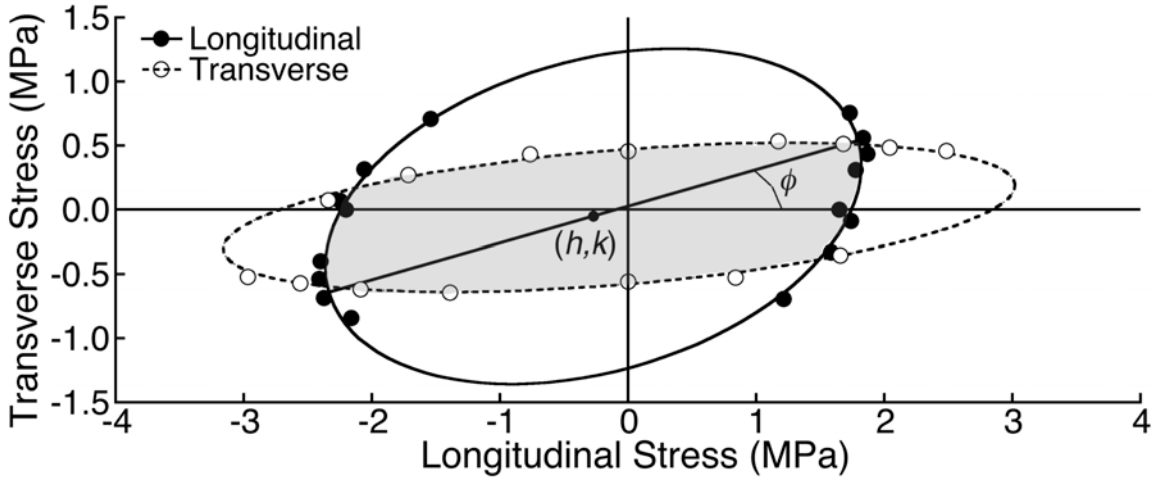

Figure 3-2: The longitudinal (solid) and transverse (open) yield points and the respective yield ellipses for one specimen. Each ellipse is represented by five parameters, the major and minor diameters (*a and b, respectively*), the coordinates of the center (*h,k*), and the angle of tilt of the major axis with respect to the horizontal (ϕ). The shaded region bounded by the two intersecting ellipses defines the elastic region.

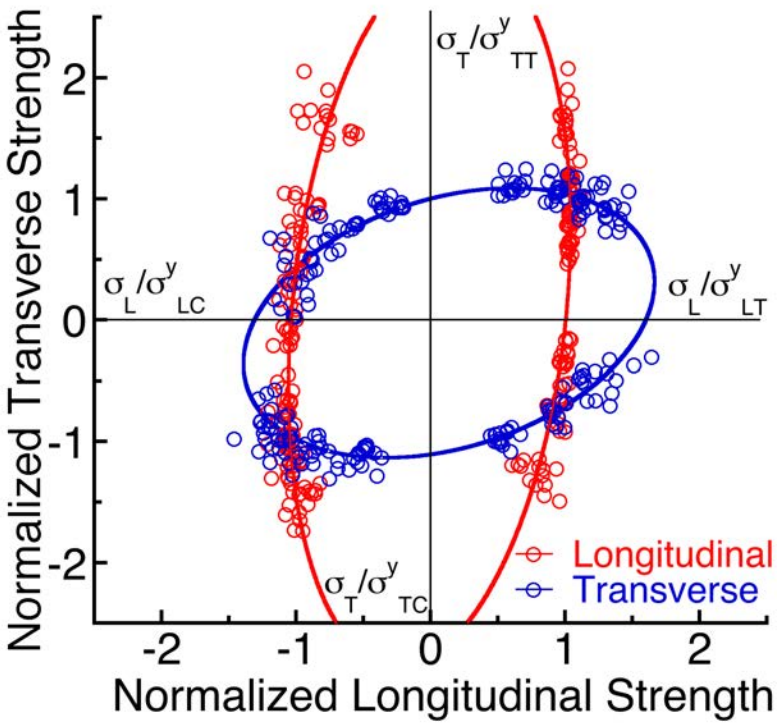

Figure 3-3: A dual-ellipse fit to the normalized longitudinal and transverse yield strength data pooled from all specimens. The yield strength in each quadrant was normalized by the respective uniaxial strengths of a given specimen.

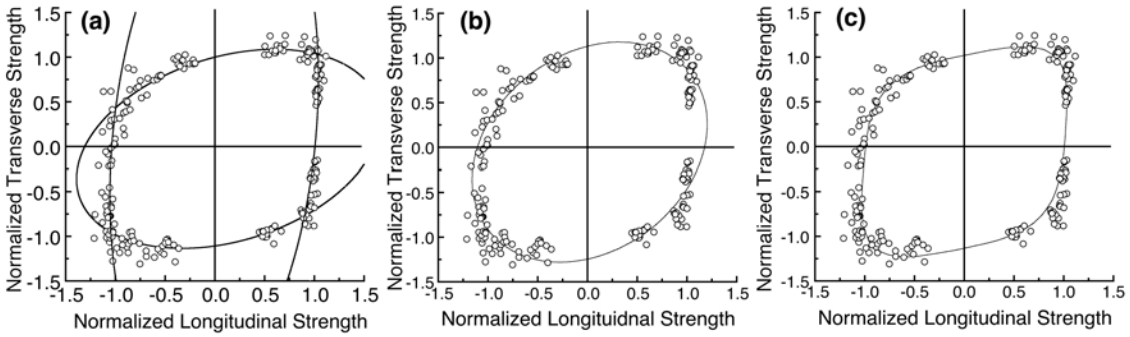

Figure 3-4: (a) Dual-Ellipse Fit (b) Single Ellipse Fit and (c) Quartic Super-Ellipse Fit to the pooled normalized chronological yield strength data.

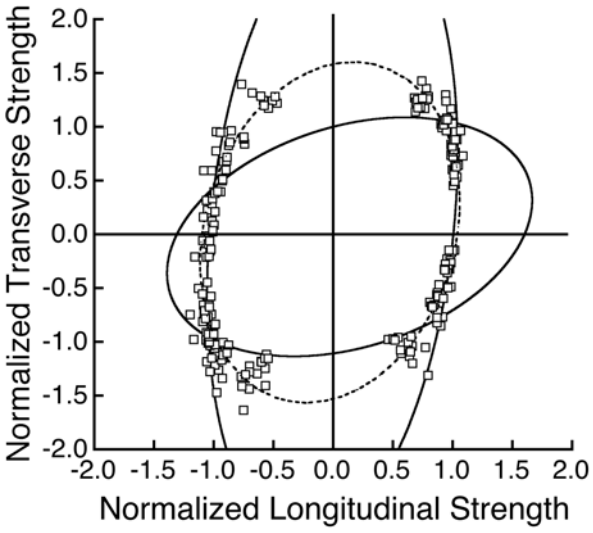

Figure 3-5: Comparison of dual-ellipse fit (solid) and a quadratic fit (dotted) to the pooled normalized equivalent yield strength data.

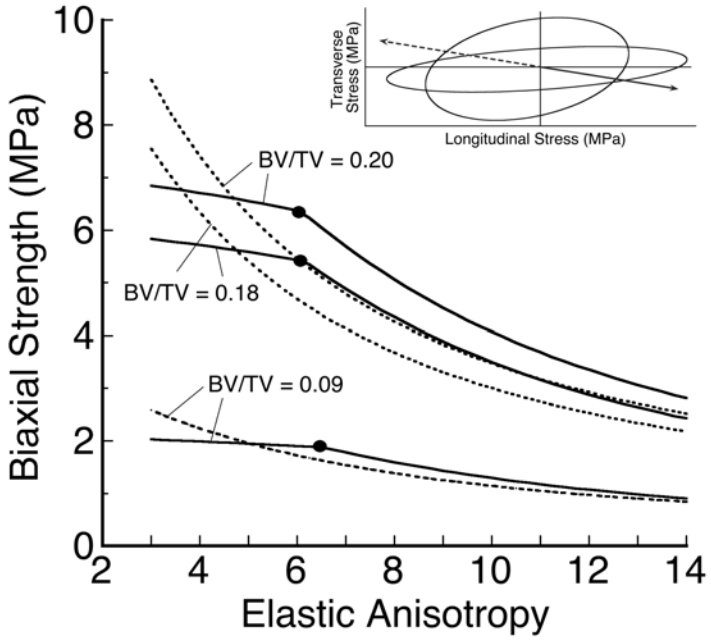

Figure 3-6: Variation of biaxial strength with elastic anisotropy at a constant bone volume fraction of 0.09, 0.18 and 0.20 for two biaxial loading cases: longitudinal compression and transverse tension in a ratio of 5:1 (dotted line) and longitudinal tension and transverse compression, also in a ratio of 5:1 (solid line). For longitudinal compression and transverse tension, biaxial strength was defined by the transverse direction. For longitudinal tension and transverse compression, the biaxial strength was defined by the longitudinal direction up to an elastic anisotropy of ~6, beyond which the biaxial strength was defined by the transverse direction.

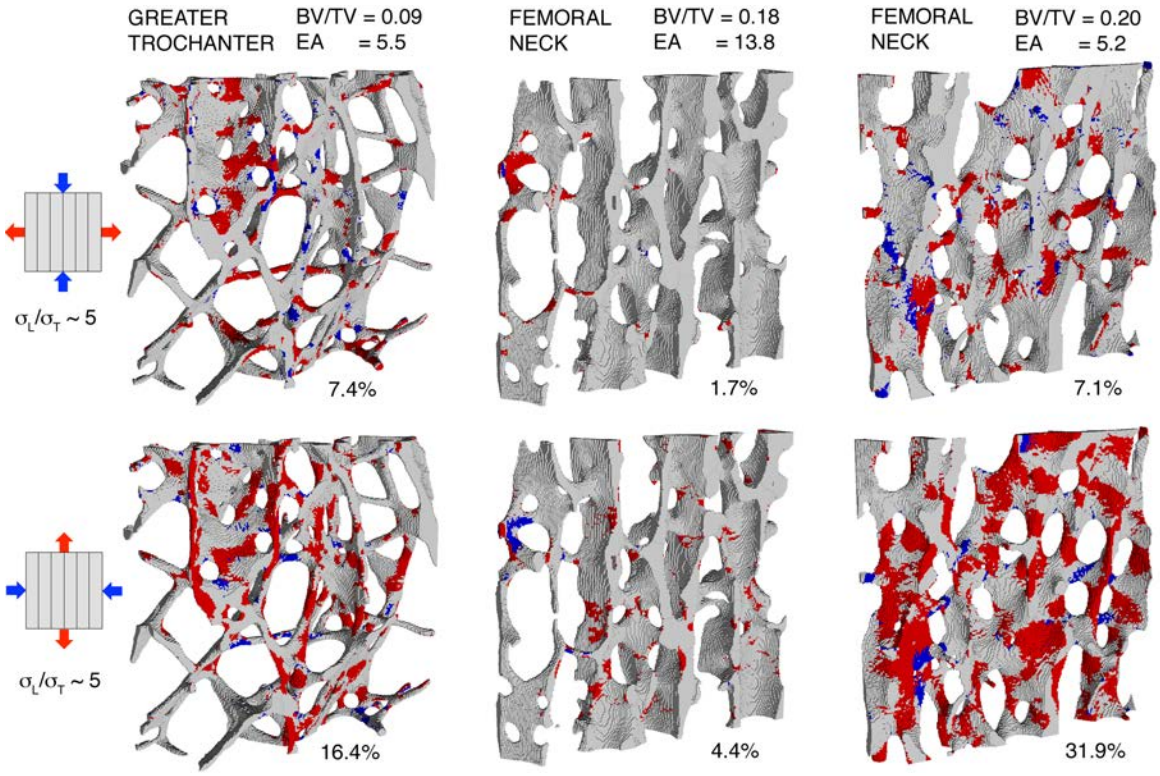

Figure 3-7: Distribution of failed tissue at the biaxial yield point in thin (~0.45 mm) longitudinal slices taken from three 5-mm cube specimens subjected to two biaxial loading cases (top row: longitudinal compression and transverse tension in a ratio of about 5:1; bottom row: longitudinal tension and transverse compression, also in a ratio of about 5:1). The percentage value denotes the proportion (percentage) of total tissue failed in the overall cube specimen at the biaxial yield point. Red regions denote tissue failed in tension and blue regions denote tissue failed in compression.

4. MULTI-AXIAL STRENGTH CRITERION OF HUMAN TRABECULAR BONE

4.1. Introduction

Although the structure of trabecular bone is primarily adapted to sustain uniaxial loads along its principal material orientation, it can be subjected to multi-axial loads in vivo, during traumatic activities such as fall and during surgical procedures such as bone grafts and joint arthoplasty [38, 98, 99]. The multi-axial strength behavior has been studied for bovine and human trabecular bone using both experiments [43] [19, 22, 26] and micro-CT based finite element simulations [23, 24, 27]. Based on these studies, various failure criterion such as the fabric anisotropy based Tsai-Wu failure criterion [21, 27], the piecewise Hill's criterion [25, 26, 100] and the modified super-ellipsoid criterion [24] have been proposed. Such multi-axial failure criteria have been used in clinical studies to non-invasively predict strength of whole bones and their susceptibility to fracture using QCT-based finite element models [101, 102].

Trabecular bone is often idealized as a cellular structure consisting of a network of rods and plates[103], and therefore its multi-axial mechanical behavior is similar to that of other cellular materials such as polymeric foams [28, 104, 105]. While some studies have used the quadratic Tsai-Wu failure criterion [20] to define the multi-axial failure behavior of foams [106] and trabecular bone [27], other studies on foams [29, 85, 107] and trabecular bone [24], suggest that the failure under multi-axial loads may not quadratic. The biaxial study (*Chapter 3*) established that the behavior for trabecular bone is decoupled in the longitudinal and transverse direction due to its anisotropic and porous nature and therefore the biaxial yield behavior in the axial-transverse plane is not quadratic and could possibly be quartic in nature. It was also found that the variation in biaxial strength due to bone volume fraction, anisotropy and microarchitecture after accounting for such variations in the uniaxial strength, is minor. Therefore, based on our results of the biaxial study, the overall goal of this study was to define a complete three-dimensional multi-axial yield strength criterion of human trabecular bone from various anatomic sites covering a wide range of bone volume fraction and microarchitecture.

4.2. Methods

For this study, micro-computed tomography (μCT-20, Scanco Medical AG, Bassersdorf, Switzerland) images—10μm spatial resolution—of 10 human trabecular bone specimens were obtained (cadaver age=64±10, 48-79; 3 female, 7 male), from three anatomic sites: vertebral body (n=3), femoral neck (n=5), and proximal tibia (n=2). These specimens were originally machined as 8mm-diameter cylindrical cores along their principal material orientation. A 5-mm cube was virtually extracted from the images of the cylindrical specimen and finite element model was created for each specimen by converting each bone voxel to a solid brick element with an element size of 20μm to ensure numerical convergence [51, 108]. The Euler angles of misalignment were calculated by conducting six uniaxial linear elastic finite element analyses [52]; the angle of misalignment of each specimen from the orthotropic axes was confirmed to be within

$\pm 10^0$, ensuring the extracted cube specimens were adequately aligned with the principal orthotropic trabecular orientation. The elastic moduli in the longitudinal direction (E_3) and the transverse directions (E_2, E_1, $E_2 > E_1$) were calculated and three anisotropy ratios (E_3/E_1, E_3/E_2, E_2/E_1) were defined for each specimen. The cohort of 10 specimens covered a wide range of bone volume fraction (BV/TV=0.19±0.09, range=0.09-0.36) and anisotropy ratios (E_3/E_1=6.7±3.1, range=3.0-12.0; E_3/E_2=3.7±2.1; range=2.1-7.6; E_2/E_1=1.9±0.7; range=1.2-3.1).

For all nonlinear analyses, all finite elements were assigned the same hard tissue material properties having an isotropic elastic modulus of 18.0 GPa, a Poisson's ratio of 0.3, and a rate-independent elastic-plastic material model [53] with geometric kinematic non-linearity and tension-compression strength asymmetry of the bone tissue. [47].

The yield surface was obtained in the three-dimensional normal strain and stress space and in the nine normal-shear strain planes by analyzing various multi-axial loading cases for each specimen. Nonlinear (geometrically and materially) finite element analysis was conducted using proportional loading where each loading case was uniquely defined by the maximum strains applied in each direction for a total of 231 loading cases (**Table 4-1**) per specimen. For each loading case, stress-strain curves were obtained in each direction and 0.2% offset yield strains were calculated. The first chronological yield point—in loading history—was used to define the multi-axial yield stress and yield strain as done in previous studies [24]. The yield stress and yield strain data from the multi-axial analyses were normalized by the three uniaxial yield stresses and six uniaxial yield strains respectively to define the normalized normal strain, normalized shear strain and normalized normal stress as follows:

$$\hat{\varepsilon}_{ij} = \begin{cases} \dfrac{\varepsilon_{ij}}{\left|\varepsilon_{ij}^{yt}\right|}, \varepsilon_{ij} > 0 \\ \dfrac{\varepsilon_{ij}}{\left|\varepsilon_{ij}^{yc}\right|}, \varepsilon_{ij} < 0 \end{cases} \qquad \hat{\gamma}_{ij} = \frac{\gamma_{ij}}{\gamma_{ij}^{y}} \qquad \hat{\sigma}_{ij} = \begin{cases} \dfrac{\sigma_{ij}}{\left|\sigma_{ij}^{yt}\right|}, \sigma_{ij} > 0 \\ \dfrac{\sigma_{ij}}{\left|\sigma_{ij}^{yc}\right|}, \sigma_{ij} < 0 \end{cases}$$

where $\varepsilon_{ij}, \gamma_{ij}, \sigma_{ij}$ (i,j,k=1,2,3) are normal strain, shear strain and normal stress respectively and the quantities with subscript *yt* and *yc* are the uniaxial yield strain/stress in tension and compression respectively. The regressions of the yield quantities with bone volume fraction and anisotropy ratios were calculated (**Table 4-2**) (microarchitecture did not have significant effect).

The finite element-computed yield data in the strain space, normalized strain space and normalized stress space, were fit to various criteria in order to identity which criterion best fit the observed behavior (by finite element analysis). For each criterion, an error norm between the criterion and the finite element data was calculated for each finite element simulation, as follows

$$\frac{\left\| \underline{x}_{predicted} - \underline{x}_{FE} \right\|}{\left\| \underline{x}_{FE} \right\|} \times 100$$

in which $\underline{x}_{predicted}$ is the predicted yield point from the fitted criterion and $\underline{x}_{FE}$ is the finite element-computed yield point. For each criterion, this error norm was first averaged over all simulations for each specimen, and then averaged again over all ten specimens. Unless noted otherwise, the latter averaged error is reported (the reported SD is that describing the variation of the specimen-specific average values across the ten specimens). Also, unless noted otherwise, we report errors for both a specimen-specific criterion, in which any fitted coefficients in the criterion are specific to an individual specimen, and an averaged criterion, in which any fitted coefficients in the criterion are averaged across all specimens and therefore are not specific to an individual specimen.

The finite element-computed yield data in the normal strain space of each specimen was fit to three criteria. The first criterion evaluated was the nine-coefficient "modified super-ellipsoid" yield criterion [24], formulated in normal strain space:

$$g\left(\varepsilon_{11},\varepsilon_{22},\varepsilon_{33}\right)=\left[\left|\frac{\varepsilon_{11}-c_1}{r_1}\right|^{2/n_2}+\left|\frac{\varepsilon_{22}-c_2}{r_2}\right|^{2/n_2}\right]^{n_2/n_1}+\left|\frac{\varepsilon_{33}-c_3}{r_3}\right|^{2/n_1}+\left|\frac{t\left(\varepsilon_{11}+\varepsilon_{22}+\varepsilon_{33}\right)}{r_1+r_2+r_3}\right|^{2/n_1}-1 \qquad \textit{(Equation 4-1)}$$

We used the previously published coefficients of the criterion to prospectively test the published criterion to the data generated in this study. In addition, we calibrated this criterion using data from the current study to define specimen-specific coefficients for each specimen. The second criterion was a "quartic" yield criterion, which was mathematically similar to the modified super-ellipsoid criterion:

$$g\left(\varepsilon_{11},\varepsilon_{22},\varepsilon_{33}\right)=\left(\frac{\varepsilon_{11}-c_1}{r_1}\right)^4+\left(\frac{\varepsilon_{22}-c_2}{r_2}\right)^4+\left(\frac{\varepsilon_{33}-c_3}{r_3}\right)^4+\left(\frac{t_1\varepsilon_{11}+t_2\varepsilon_{22}+t_3\varepsilon_{33}}{r_1+r_2+r_3}\right)^4-1 \qquad \textit{(Equation 4-2)}$$

Here ε_{11}, ε_{22}, ε_{33} are normal strains (in percentage) and (c_1, c_2, c_3, r_1, r_2, r_3, t_1, t_2, t_3) are the parameters of the equation. The criterion was evaluated in specimen-specific form (using specimen-specific coefficients) and also in averaged form. For the latter, the mean value of the specimen-specific coefficients for the ten specimens was calculated for each of the nine coefficients, and the resulting mean values were then used to define a single, averaged quartic yield criterion in the normal strain space (**Table 4-3**). The third criterion evaluated, included for reference purposes, was the nine-coefficient quadratic Tsai-Wu criterion [20], evaluated in both specimen-specific and averaged form:

$$g(\varepsilon_{11},\varepsilon_{22},\varepsilon_{33}) = F_i\varepsilon_{ii} + F_{ij}\varepsilon_{ii}\varepsilon_{jj} - 1 \qquad (i, j = 1,2,3) \qquad \textit{(Equation 4-3)}$$

On observing that the quartic yield criterion was a good fit to the normal strain data, we extended it to include both normal (ε_{ij}) and shear (γ_{ij}) strains and formulated it in (six-dimensional) normalized strain space ($\hat{\varepsilon}_{11},\hat{\varepsilon}_{22},\hat{\varepsilon}_{33},\hat{\gamma}_{12},\hat{\gamma}_{23},\hat{\gamma}_{13}$):

$$g(\hat{\underline{\varepsilon}}) = \left[\frac{\hat{\varepsilon}_{11} - c_1}{r_1}\right]^4 + \left[\frac{\hat{\varepsilon}_{22} - c_2}{r_2}\right]^4 + \left[\frac{\hat{\varepsilon}_{33} - c_3}{r_3}\right]^4 + \left[\frac{t_1\hat{\varepsilon}_{11} + t_2\hat{\varepsilon}_{22} + t_3\hat{\varepsilon}_{33}}{r_1 + r_2 + r_3}\right]^4 + \left[\frac{u_1\hat{\varepsilon}_{11} + v_1\hat{\gamma}_{23} + w_1(\hat{\gamma}_{13} + \hat{\gamma}_{12})}{r_1 + r_2 + r_3}\right]^4 +$$
$$\left[\frac{u_2\hat{\varepsilon}_{22} + v_2\hat{\gamma}_{13} + w_2(\hat{\gamma}_{12} + \hat{\gamma}_{23})}{r_1 + r_2 + r_3}\right]^4 + \left[\frac{u_3\hat{\varepsilon}_{33} + v_3\hat{\gamma}_{12} + w_3(\hat{\gamma}_{13} + \hat{\gamma}_{23})}{r_1 + r_2 + r_3}\right]^4 - 1 \qquad \textit{(Equation 4-4)}$$

in which c_1, c_2, c_3, r_1, r_2, r_3, t_1, t_2, t_3, u_1, u_2, u_3, v_1, v_2, v_3, w_1, w_2, and w_3 are the fitted coefficients. This 18-coefficient criterion was first fit in a specimen-specific manner. The 18 coefficients obtained for each specimen were correlated to bone volume fraction, microarchitecture and anisotropy ratios and regression equations were obtained for each of these parameters (**Table 4-4**). In addition, the mean value of the specimen-specific coefficients for the ten specimens were used to define a single, averaged quartic yield criterion in the normalized strain space.

Since the quartic yield criterion (*equation 4-4*) did not fit the normalized normal-shear strain yield data in the $\hat{\varepsilon}_{33} - \hat{\gamma}_{13}$ $\hat{\varepsilon}_{33} - \hat{\gamma}_{23}$ planes, based on previously published experimental work on axial-shear behavior [19], the finite element-computed normalized normal-shear strain data in the $\hat{\varepsilon}_{33} - \hat{\gamma}_{13}$ $\hat{\varepsilon}_{33} - \hat{\gamma}_{23}$ planes was fit to two linear fits to define a linear yield criterion of the form:

$\hat{\gamma}_{i3} = r_{ic}\hat{\varepsilon}_{33} + s_{ic}$ (i=1,2) in the compression quadrant and
$\hat{\gamma}_{i3} = r_{it}\hat{\varepsilon}_{33} + s_{it}$ (i=1,2) in the tension quadrant *(Equation 4-5)*

where r_{ic}, r_{it}, s_{ic}, s_{it} (i = 1,2) are 8 parameters equivalent to the slope and intercept of the linear fits. The linear yield criterion was fit individually for each specimen and specimen-specific coefficients were obtained. These coefficients were correlated to bone volume fraction, microarchitecture and anisotropy ratios. The mean value of the specimen-specific coefficients for the ten specimens were then used to define a single, averaged linear yield criterion in the normalized normal-strain space in the $\hat{\varepsilon}_{33} - \hat{\gamma}_{13}$ $\hat{\varepsilon}_{33} - \hat{\gamma}_{23}$ planes. Therefore, the full multi-axial yield behavior in the normalized strain space was defined as the combination of the quartic yield criterion (*equation 4-4*) and the linear yield criterion (*equation 4-5*).

In the normalized stress space, the following equation was fit to the finite element-computed normalized yield stress data for each specimen:

$$f(\hat{\sigma}_{11}, \hat{\sigma}_{22}, \hat{\sigma}_{33}) = \left(\frac{\hat{\sigma}_{11} - c_1}{r_1}\right)^4 + \left(\frac{\hat{\sigma}_{22} - c_2}{r_2}\right)^4 + \left(\frac{\hat{\sigma}_{33} - c_3}{r_3}\right)^4 + \left(\frac{t_1\hat{\sigma}_{11} + t_2\hat{\sigma}_{22} + t_3\hat{\sigma}_{33}}{r_1 + r_2 + r_3}\right)^4 +$$
$$\left(\frac{m_1\hat{\sigma}_{11} + m_2\hat{\sigma}_{22}}{r_1 + r_2}\right)^4 + \left(\frac{n_2\hat{\sigma}_{22} + n_3\hat{\sigma}_{33}}{r_2 + r_3}\right)^4 + \left(\frac{p_1\hat{\sigma}_{11} + p_3\hat{\sigma}_{33}}{r_1 + r_3}\right)^4 - 1 \qquad \textit{(Equation 4-6)}$$

where $\hat{\sigma}_{11}, \hat{\sigma}_{22}, \hat{\sigma}_{33}$ are the normalized normal stresses and (c_1, c_2, c_3, r_1, r_2, r_3, t_1, t_2, t_3, m_1, m_2, n_2, n_3, p_1, p_3) are 15 coefficients of the equation. For reference purposes, a quadratic yield criterion (*equation 4-3*) was also fit to the normalized stress data for each specimen.

4.3. Results

For the three biaxial planes, the distribution of the finite element-generated yield points resembled a box-like shape in the normalized strain space ($\hat{\varepsilon}_{11}-\hat{\varepsilon}_{22}, \hat{\varepsilon}_{22}-\hat{\varepsilon}_{33}$, $\hat{\varepsilon}_{11}-\hat{\varepsilon}_{33}$) (**Figure 4-1**). The scatter in these failure data across specimens was reduced substantially, when the failure data were expressed as normalized strains (**Figure 4-1**, *middle panel*) versus (un-normalized) strains (**Figure 4-1,** *top panel*) or normalized stresses (**Figure 4-1**, *bottom panel*), particularly in the transverse $\hat{\sigma}_{11}-\hat{\sigma}_{22}$ plane. The normalized normal-shear yield strain data also displayed some scatter especially in the $\hat{\varepsilon}_{11}-\hat{\gamma}_{12}, \hat{\varepsilon}_{11}-\hat{\gamma}_{13}, \hat{\varepsilon}_{22}-\hat{\gamma}_{12}, \hat{\varepsilon}_{22}-\hat{\gamma}_{13}$ transverse planes (**Figure 4-2**). In the normalized normal-shear strain space, the distribution of yield points in the $\hat{\varepsilon}_{11}-\hat{\gamma}_{23}$, $\hat{\varepsilon}_{22}-\hat{\gamma}_{13}, \hat{\varepsilon}_{33}-\hat{\gamma}_{12}$ planes resembled a rectangular box-like shape, in the $\hat{\varepsilon}_{11}-\hat{\gamma}_{12}$, $\hat{\varepsilon}_{11}-\hat{\gamma}_{13}$, $\hat{\varepsilon}_{22}-\hat{\gamma}_{12}$, $\hat{\varepsilon}_{22}-\hat{\gamma}_{23}$ planes resembled a rhomboidal box-like shape, whereas in the $\hat{\varepsilon}_{33}-\hat{\gamma}_{13}$, $\hat{\varepsilon}_{33}-\hat{\gamma}_{23}$ planes resembled a triangular shape (**Figure 4-2**).

The error of the specimen-specific fits of the modified super-ellipsoid criterion (*equation 4-1*), the quartic yield criterion (*equation 4-2*) and the quadratic Tsai-Wu criterion (*equation 4-3*) 4.2±0.6% , 3.5±0.5% and 8.0±0.4% respectively. The error of fit of the single, averaged quartic yield criterion based on the mean value of coefficients listed in Table 4-3 was 5.3±1.5%, whereas the error of fit of the modified super-ellipsoid equation (*equation 4-1*) with previously published coefficients [24] was 5.6±1.6%, suggesting that the quartic equation gives an equally good fit as the modified super-ellipsoid criterion.

The six-dimensional quartic yield criterion (*equation 4-4*) in the normalized strain space gave a good fit to the finite element-computed normalized yield points with a mean error of 4.0±0.7% across all specimens. The error in the normalized normal strain space was 3.7±0.6%. In the normalized axial-shear strain space, the error was much larger in $\hat{\varepsilon}_{33}-\hat{\gamma}_{13}$, $\hat{\varepsilon}_{33}-\hat{\gamma}_{23}$ planes (7.5±1.8%) compared to the other axial-shear planes (3.3±0.8%). Combining the quartic yield criterion (*equation 4-4*) and the linear yield criterion (*equation 4-5*), the error in $\hat{\varepsilon}_{33}-\hat{\gamma}_{13}$ and $\hat{\varepsilon}_{33}-\hat{\gamma}_{23}$ planes reduced to 2.4±0.5%. While some of the 18 coefficients of the quartic yield criterion (*equation 4-4*) depended weakly on the bone volume fraction and/or the anisotropy ratios (**Table 4-4**), the 8 coefficients of the linear yield criterion (*equation 4-5*) did not depend on the bone volume fraction, microarchitecture or anisotropy ratios (**Table 4-5**). The average single quartic yield criterion based on mean value of coefficient listed in Table 4-4, along with the average single linear yield based on mean value of coefficients listed in Table 4-5, resulted in an error of 4.8±0.7%.

In the normalized stress space, the mean error of fit of the quartic yield criterion (*equation 4-5*) to the finite-element computed normalized normal stress data was 4.1±0.7%, whereas for the quadratic yield criterion was 5.6±0.7%.

4.4. Discussion

The result of this computational study suggests that a combination of a quartic yield criterion and a linear yield criterion can be used to define the multi-axial yield behavior of human trabecular bone after accounting for variations in the uniaxial yield strengths due to bone volume fraction, anisotropy and microarchitecture. The yield behavior is homogeneous in the normalized strain space with negligible inter-specimen variations. However, there is a greater degree of heterogeneity in yield behavior in the normalized stress space. We therefore propose the multi-axial yield criterion in the six-dimensional normalized strain space for human trabecular bone.

The form of the proposed quartic yield criterion proposed captures the interaction between the three normal strains and three shear strains. In the normalized normal strain space, there is little interaction of the longitudinal normal strain and the transverse normal strains, which leads to a rectangular box-like flat shape of the yield surface, whereas there is some degree of interaction in transverse plane, which leads to a slightly rhomboidal shape of the yield surface. In the normalized normal-shear strain space, the interaction is minimal when the normal strain is out of the plane of shear (i.e. $\hat{\varepsilon}_{11}-\hat{\gamma}_{23}$, $\hat{\varepsilon}_{22}-\hat{\gamma}_{13}$, $\hat{\varepsilon}_{33}-\hat{\gamma}_{12}$) leading to a rectangular flat box-like shape, whereas the interaction of the normal and shear strains is higher when the normal strain is in the plane of shear leading to either a rhomboidal box-like shape when normal strain is in the transverse plane (i.e. $\hat{\varepsilon}_{11}-\hat{\gamma}_{12}$, $\hat{\varepsilon}_{11}-\hat{\gamma}_{13}$, $\hat{\varepsilon}_{22}-\hat{\gamma}_{12}$, $\hat{\varepsilon}_{22}-\hat{\gamma}_{23}$) or a triangular shape when the normal strain is in the longitudinal direction (i.e. $\hat{\varepsilon}_{33}-\hat{\gamma}_{13}$, $\hat{\varepsilon}_{33}-\hat{\gamma}_{23}$). The proposed quartic yield criterion is able to capture the rectangular or rhomboidal shape of the yield surface but is unable to capture the triangular shape in the two normalized axial-shear planes. The triangular shape of the yield surface in these planes has been observed previously in axial-torsion experiments on bovine trabecular bone [19]. While the rectangular shape of yield surface due to decoupling of the normal and shear loading modes is straightforward and has been discussed previously [24], the two different shapes of yield surface observed when the normal and shear loading modes are coupled can be explained by the fact that in the $\hat{\varepsilon}_{33}-\hat{\gamma}_{13}$, $\hat{\varepsilon}_{33}-\hat{\gamma}_{23}$ planes, the multi-axial yield is dominated by the shear direction which leads to a triangular shape, whereas in the $\hat{\varepsilon}_{11}-\hat{\gamma}_{12}$, $\hat{\varepsilon}_{11}-\hat{\gamma}_{13}$, $\hat{\varepsilon}_{22}-\hat{\gamma}_{12}$, $\hat{\varepsilon}_{22}-\hat{\gamma}_{23}$ planes, the multi-axial yield is dominated by the normal direction which leads to a rhomboidal shape. We therefore defined a linear yield criterion specifically for loading in the $\hat{\varepsilon}_{33}-\hat{\gamma}_{13}$, $\hat{\varepsilon}_{33}-\hat{\gamma}_{23}$ planes, whereas the quartic yield criterion worked well for all other loading cases.

The effect of applying displacement-controlled boundary condition on porous and heterogeneous trabecular bone cube specimens resulted in more heterogeneity in the normalized yield stress data compared to the normalized yield strain data. This can be explained by the unconfined nature of the stress simulations which allow the trabeculae at the edges to deform freely and independently of each other resulting in more scatter as

opposed to confined nature of the strain simulations which restrict the trabeculae at the edges to deform together in a predetermined manner resulting in much less scatter. The small overshoot of the biaxial normal yield stress data near the uniaxial axes, can be explained by the stiffening effect of a biaxial stress simulation when four faces of the cube are constrained over a uniaxial stress simulation when only two faces of the cube are constrained. In addition, the large scatter in the $\hat{\sigma}_{11} - \hat{\sigma}_{22}$ transverse plane can be attributed to the thin trabeculae in the transverse plane undergoing large deformations. Due to the large scatter in the normalized stress space, the quartic yield criterion required 15 parameters as opposed to 9 parameters in normalized strain space. Therefore, the yield strength analyses in the axial-shear stress space were not pursued.

Our results are supported by previous studies. The multi-axial failure of foams has been characterized previously [28] using a quartic equation that gives the failure envelope a box-like shape for a biaxial loading. Similarly, a quartic yield surface has been proposed for anisotropic plates [109] and other researchers have proposed non-quadratic yield criteria for anisotropic metals [110, 111] and foams [85] that include higher order terms to capture the flat regions of the yield surface. Gol'denblat and Kopnov [112] had proposed a generalized tensor polynomial criterion, the quadratic version of which proposed by Tsai and Wu [20] has been widely used for anisotropic materials. While yield criteria of quadratic form [20, 113-116] are widely used in computational studies, our results clearly suggest that use of higher order terms better captures the multi-axial yield behavior of trabecular bone. Bower and Koedam [117] have explored the application of quadratic, cubic and quartic versions of the generalized tensor polynomial failure criterion and suggested the use of the quartic version for convexity requirements. The form of the six-dimensional quartic yield criterion proposed in this study is similar to the modified super-ellipsoid yield criterion, but when expanded, it can be written in a quartic tensor polynomial form as follows:

$$F_i\hat{\varepsilon}_i + F_{ij}\hat{\varepsilon}_i\hat{\varepsilon}_j + F_{ijk}\hat{\varepsilon}_i\hat{\varepsilon}_j\hat{\varepsilon}_k + F_{ijkl}\hat{\varepsilon}_i\hat{\varepsilon}_j\hat{\varepsilon}_k\hat{\varepsilon}_l$$

where (i, j, k, l = 1,2,3,4,5,6). The suggested form of the proposed six-dimensional quartic yield criterion also ensures its convexity, which is a desirable numerical trait in the implementation of plasticity algorithms.

This study has some limitations. First, the use of small cube specimens of trabecular bone results in truncated trabeculae at the edges that induces side-artifact effects [118]. In addition, the small size of the cubes can overestimate the effective mechanical properties [72, 119] due to suppression of large deformation bending of truncated trabeculae. A second major limitation of the study was that the form of the proposed quartic yield criterion did not capture the yield behavior in two normal-shear planes and we had to define a piecewise yield criterion in these two planes. An alternative could be to explore the form of the full quartic tensor polynomial yield criterion subjected to the convexity constraints on the coefficients [117] which could provide more flexibility in the variation of the yield surface in different planes. Thirdly, the angle of misalignment of a few specimens was close to 10^0, which could have caused some scatter in the normalized normal-shear strain space and the normalized stress space. Lastly,

although the multi-axial failure criterion was proposed in the principal orthotropic coordinate system with loading along the main trabecular orientation, the applicability of this criterion for off-axis loading [18] scenario remains open for investigation.

Table 4-1: Details of Multi-axial Analyses

Type of Analysis / Boundary Condition	Analysis Details	Number of Analysis
Normal Strain and Normal Stress Analyses		
Uniaxial Strain	3 Directions: Tension + Compression	6
Biaxial Strain	(3 biaxial planes) x (4 quadrants per plane) x (3 analysis per quadrant)	36
Uniaxial Stress	3 Directions: Tension + Compression	6
Biaxial Stress	(3 biaxial planes) x (4 quadrants per plane) x (3 analysis per quadrant)	36
Triaxial Stress/Strain	(8 octants) x (9 analysis per octant)	72
		156
Normal-Shear Strain Analysis		
Shear Strain	3 Directions	3
Axial-Shear Biaxial Strain	(9 planes) x (2 quadrants per plane) x (4 analysis per quadrant)	72
		75

Table 4-2: Multivariate regression of uniaxial yield strains (in percentage) and uniaxial yield stresses (in MPa) with bone volume fraction and anisotropy ratios of the form $Y = a_0 + a_1(BV/TV) + a_2(E_3/E_1) + a_3(E_3/E_2) + a_4(E_2/E_1)$ for the yield strains and the form $Y= a_0(BV/TV)^{a1}(E_3/E_1)^{a2}(E_3/E_2)^{a3}(E_2/E_1)^{a4}$ for the yield stresses. The mean values are listed in the last column. By convention, direction 3 is the longitudinal direction and directions 1 and 2 are in the transverse plane, such that the elastic modulus are ordered as $E_3 > E_2 > E_1$

Y	a_0	a_1	a_2	a_3	a_4	R^2	Mean
ε_{11}^{yt}	0.683	0	0	0	0	-	0.683
ε_{22}^{yt}	0.582	0	0	0.0152	0	0.46	0.639
ε_{33}^{yt}	0.582	0	0	0	0	-	0.582
ε_{11}^{yc}	0.909	0	0	0	0	-	0.909
ε_{22}^{yc}	0.952	0	0	0	-0.0476	0.43	0.860
ε_{33}^{yc}	0.816	0.278	0	0	0	0.69	0.871
γ_{12}^{y}	1.21	0	0	0	0	-	1.21
γ_{23}^{y}	1.10	0	0	0	0	-	1.10
γ_{13}^{y}	1.13	0	0	0	0	-	1.13
σ_{11}^{yt}	53.9	1.46	-0.658	0	0	0.98	2.03
σ_{22}^{yt}	70.9	1.57	0	-0.632	0	0.99	3.20
σ_{33}^{yt}	73.2	1.46	0	0	0	0.97	7.19
σ_{11}^{yc}	105	1.58	-0.752	0	0	0.99	2.94
σ_{22}^{yc}	131	1.64	0	-0.796	0	0.99	4.59
σ_{33}^{yc}	153	1.61	0	0	0	0.98	12.1

Table 4-3: Mean value (± SD) of the coefficients of the quartic yield criterion *(equation 4-2)* and published coefficients of the modified super-ellipsoid yield criterion *(equation 4-1)*

Quartic Criterion		Modified Super-Ellipsoid Criterion	
c_1	-0.159 (0.029)	c_1	-0.145
c_2	-0.122 (0.014)	c_2	-0.152
c_3	-0.148 (0.019)	c_3	-0.169
r_1	0.869 (0.094)	r_1	0.728
r_2	0.779 (0.031)	r_2	0.719
r_3	0.740 (0.018)	r_3	0.753
t_1	1.829 (0.555)		
t_2	1.263 (0.477)	t	1.396
t_3	1.044 (0.285)		
Exponent	4	$2/n_2$	4.695
		$2/n_1$	5.764

Table 4-4: Multivariate regression of 18 coefficeints of the quartic yield criterion (*equation 4-4*) with bone volume fraction and anisotropy ratios of the form $Y = a_0 + a_1(BV/TV) + a_2(E_3/E_1) + a_3(E_3/E_2) + a_4(E_2/E_1)$. The mean values of the parameters are listed in the last column.

Y	a_0	a_1	a_2	a_3	a_4	R^2	Mean
c_1	-0.0171	0	0	0	0	-	-0.0171
c_2	0.0176	0	-0.00658	0	0.0101	0.92	-0.00694
c_3	0.0218	0	-0.00131	0	0	0.62	0.0131
r_1	1.54	-1.65	0	0	0	0.63	1.22
r_2	1.01	0	0.00486	0	0	0.48	1.04
r_3	1.06	0	0	0	0	-	1.06
t_1	3.89	-6.21	0	0	0	0.54	2.67
t_2	1.11	0	0	0	0	-	1.11
t_3	0.689	0	0	0	0	-	0.689
u_1	0.910	0	0	0	0	-	0.910
u_2	0.986	0	0	0.112	0	0.46	1.41
u_3	2.13	0	0	0	0	-	2.13
v_1	1.11	0	0	0.104	0.567	0.79	2.59
v_2	0.513	0	0	0	0	-	0.513
v_3	0.812	0	0	0	0	-	0.812
w_1	3.60	-1.90	0	0	0	0.50	3.23
w_2	2.96	0	0	0	-0.195	0.55	2.59
w_3	3.04	-1.26	0	0	-0.305	0.78	2.20

Table 4-5: Mean value of the slope and intercepts of the linear yield criterion fits in the $\hat{\varepsilon}_{33} - \hat{\gamma}_{23}$ and $\hat{\varepsilon}_{33} - \hat{\gamma}_{23}$ planes of the form $\hat{\gamma}_{i3} = r_{ic}\hat{\varepsilon}_{33} + s_{ic}$ and $\hat{\gamma}_{i3} = r_{it}\hat{\varepsilon}_{33} + s_{it}$ (i=1,2).

	Mean
r_{1c}	1.02
s_{1c}	1.49
r_{1t}	-0.868
s_{1t}	1.12
r_{2c}	0.916
s_{2c}	1.43
r_{2t}	-0.714
s_{2t}	1.04

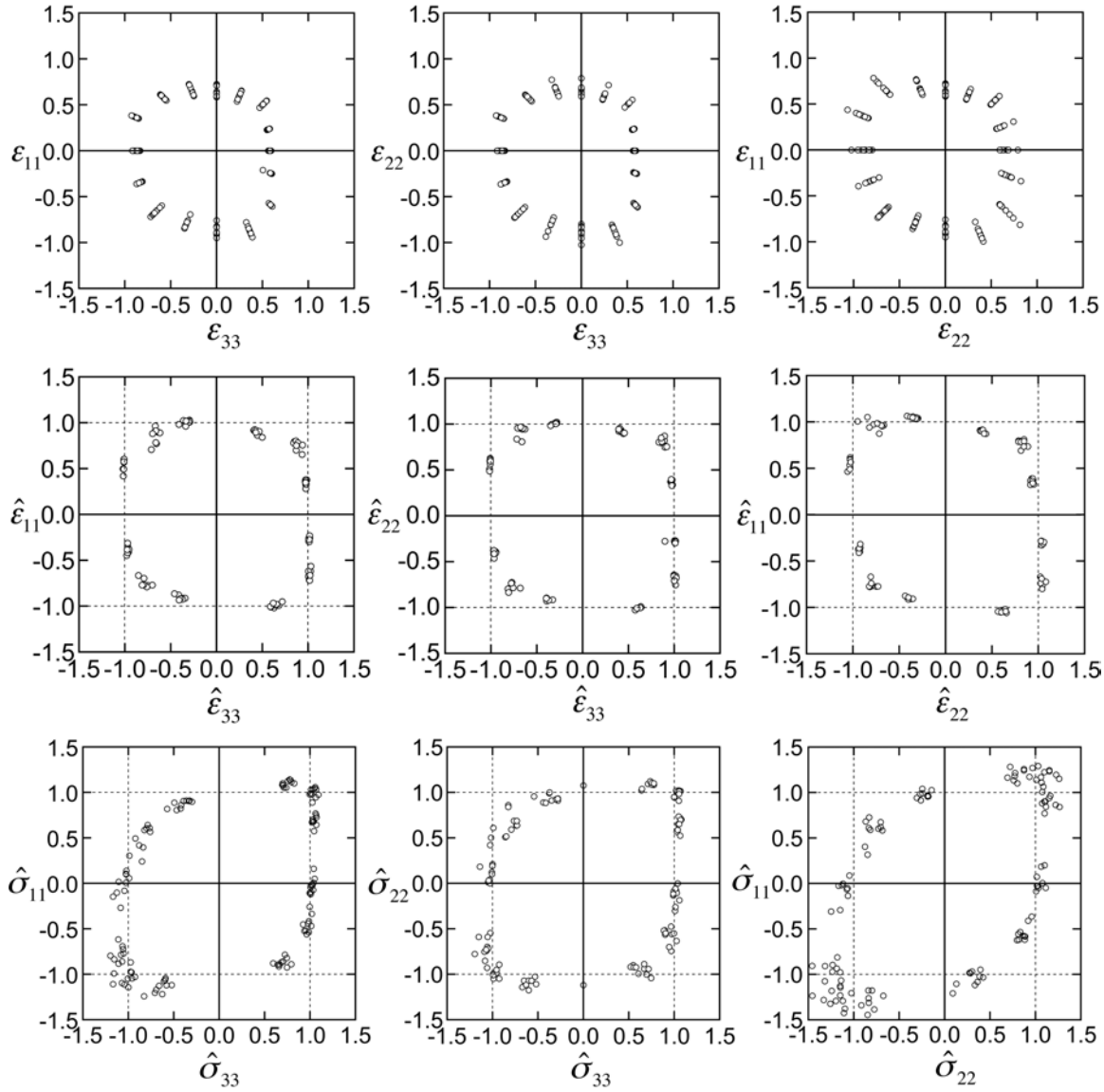

Figure 4-1: Distribution of normal yield strain data (top panel), normalized normal yield strain data (middle panel) and normalized normal yield stress data (bottom panel) from all specimens in the three normal biaxial planes.

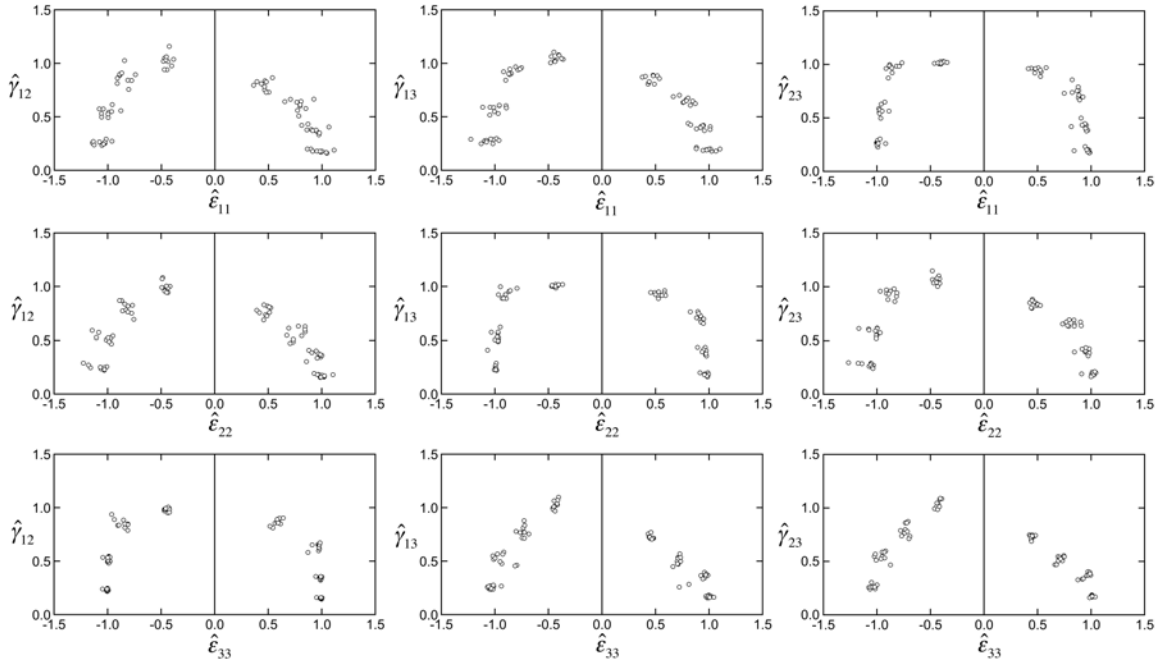

Figure 4-2: Distribution of normalized normal-shear yield strain data from all specimens in the nine normal-shear biaxial planes.

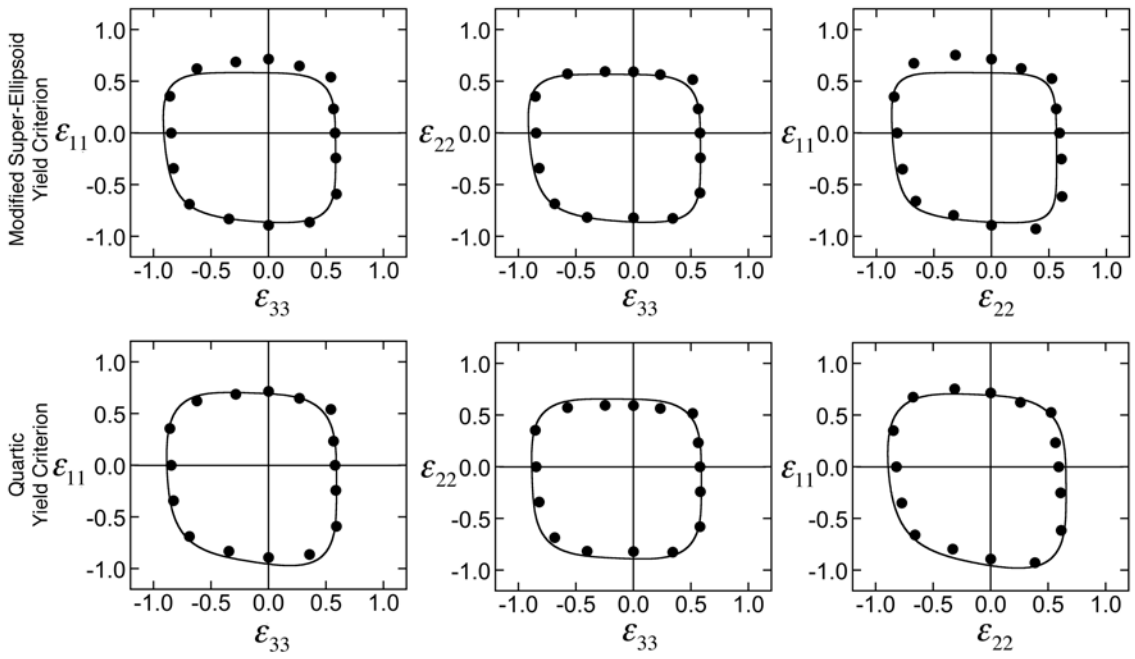

Figure 4-3: Yield envelopes in the three biaxial normal strain planes for a specimen from the vertebral body (BV/TV=0.09) using the modified super-ellipsoid criterion (*equation 4-1*) and the quartic yield criterion (*equation 4-2*).

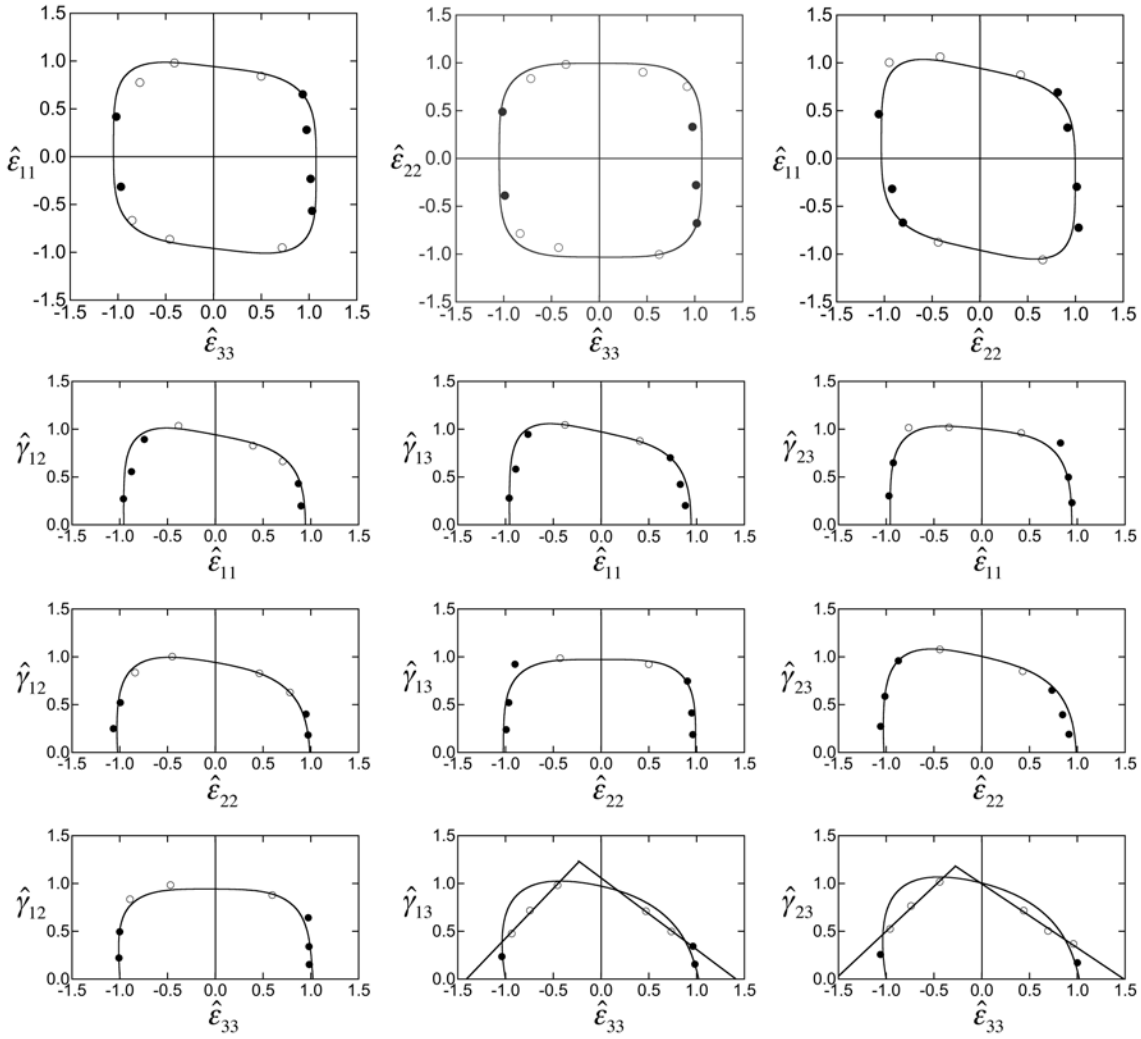

Figure 4-4: Yield envelopes in the three biaxial normalized normal strain planes and the nine normalized normal-shear strain planes for a specimen from the vertebral body (BV/TV = 0.11) using the proposed quartic yield criterion (*equation 4-4*) and linear yield criterion (*equation 4-5*). The mean error of fit of the quartic yield criterion in the $\hat{\varepsilon}_{33}-\hat{\varepsilon}_{11}$, $\hat{\varepsilon}_{33}-\hat{\varepsilon}_{22}$, $\hat{\varepsilon}_{22}-\hat{\varepsilon}_{11}$ planes was 4.2%, in the $\hat{\varepsilon}_{11}-\hat{\gamma}_{12}$, $\hat{\varepsilon}_{11}-\hat{\gamma}_{13}$, $\hat{\varepsilon}_{11}-\hat{\gamma}_{23}$, $\hat{\varepsilon}_{22}-\hat{\gamma}_{12}$, $\hat{\varepsilon}_{22}-\hat{\gamma}_{13}$, $\hat{\varepsilon}_{22}-\hat{\gamma}_{23}$, $\hat{\varepsilon}_{33}-\hat{\gamma}_{12}$ planes was 3.1% and in the $\hat{\varepsilon}_{33}-\hat{\gamma}_{13}$, $\hat{\varepsilon}_{33}-\hat{\gamma}_{23}$ planes was 7.5%. The mean error of fit of the combination of quartic and linear yield criterion in the $\hat{\varepsilon}_{22}-\hat{\gamma}_{23}$, $\hat{\varepsilon}_{33}-\hat{\gamma}_{12}$ planes was 2.4±0.5%. The solid circles fail in the mode denoted by horizontal axis and the hollow circles fail in the mode denoted by vertical axis.

5. CONCLUSIONS

In this dissertation, the strength of human trabecular bone under different loading conditions were investigated. The findings of this research are of both scientific and clinical significance: Scientifically, the high-resolution finite element models provide insight into the underlying tissue-level failure mechanisms under various loading conditions such as uniaxial compression, shear and biaxial loading. The variation of these tissue-level failure mechanisms with bone volume fraction, anisotropy and microarchitecture and their influence on the apparent-level mechanical strength properties improves the understanding of the structure-function relationship of human trabecular bone. Clinically, the mathematical characterization of the multi-axial failure behavior of human trabecular bone has the potential to improve the predictive capability of whole bone continuum-level finite element models for fracture risk assessment.

The results presented on the shear strength show that trabecular bone is especially weak under shear loading since it induces predominantly tensile tissue failure. This also holds true for any other loading condition that causes tensile tissue failure such as torsion loading. Although the shear strength of trabecular bone has been primarily characterized by testing cylindrical cores of trabecular bone under torsion loading, torsion loading induces non-uniform shear stresses in a specimen. At the microstructure level, torsion causes bending of trabeculae unlike under pure shear loading and therefore strength under torsion loading is lower than the strength under pure shear loading. At the apparent-level, the bone volume fraction of the specimen explains most of the variation in compressive, shear and torsional strengths. The trabecular microarchitecture that characterizes the heterogeneity and anisotropy of the trabecular network explains the relative difference in strength under compression and shear loading.

While the bone volume fraction, i.e. the porosity of the trabecular bone might be relevant for variation of strength under uniaxial loading conditions; the structural anisotropy also becomes relevant under biaxial loading conditions. We observed that the strength of trabecular bone when loaded along the primary trabecular orientation depends on bone volume fraction, whereas the strength when loaded transverse to the primary trabecular loading depends on both bone volume fraction and anisotropy. Therefore, the increase in anisotropy of trabecular bone is primarily due to loss of stiffness/strength in the transverse direction, which is also supported by previous studies [78, 81]. The trabecular bone in the hip and the wrist is loaded in the non-primary direction during a traumatic event such as fall, which often results in fractures in osteoporotic patients. Therefore, these results suggest that age-related changes in trabecular microarchitecture, which includes changes in anisotropy, along with age-related decrease in bone density, should be taken into account to understand the etiology of osteoporotic fractures.

The multi-axial yield behavior was found to be homogeneous in the normalized strain space when the inter-specimen variation in the uniaxial strength variations due to bone volume fraction, microarchitecture and anisotropy was decoupled from the multi-axial strength. While the yield behavior for loading in two normal-shear planes was triangular and linear in shape, the yield behavior for any other loading mode was box-like

in shape. The proposed yield criterion defined as a combination of a quartic and linear yield criterion, can be used in continuum-level finite element models obtained from clinical QCT scans to non-invasively predict strength of whole bones.

There still remain a few unanswered questions regarding the multi-axial failure behavior of trabecular bone. Firstly, the applicability of the criterion to off-axis loading needs further investigation. While the on-axis and off-axis loading of composite laminates has been investigated in many studies [120], only one study has investigated and compared the on-axis and off-axis behavior of human trabecular bone [18]. Secondly, our results are only restricted to yield strength and not ultimate strength behavior of trabecular bone. Under uniaxial loading, trabecular bone exhibits softening behavior, after reaching the ultimate stress until failure[60, 121]. The implementation of the multi-axial yield surface in continuum level finite element models should take into account the post-yield ultimate strength behavior, to accurately predict fracture of whole bones. Thirdly, the heterogeneity in the yield behavior in the stress space needs to be investigated further. It may be worthwhile exploring application of force boundary conditions for the stress-based simulations for the multi-axial behavior.

One important area of future research is the implementation of other tissue material constitutive models for trabecular bone tissue. While in this dissertation, the bone tissue was assumed to be homogeneous, isotropic with plastic behavior post-yield; in reality bone tissue is heterogeneous, anisotropic and may not be have a perfectly plastic behavior post yield. Recently, studies have investigated the post yield damage behavior of trabecular bone tissue [122, 123] and it may be worthwhile looking into effects of different post-yield behavior on the multi-axial strength. In addition, material models with viscoelastic and viscoplastic behavior should be also implemented in finite element models since high strain rate effects may be relevant for modeling impact loading of whole bones during traumatic fracture. Another important area of research would be the validation of the tissue-level failure regions with experiments on trabecular bone specimens [61, 124]. While there was some level of agreement of the tissue-level failure patterns for compression loading with previous experimental studies, the comparison was more qualitative and requires more rigorous quantitative validation of region-specific failure patterns in the trabecular bone volume.

In closure, this dissertation research has increased knowledge regarding the multi-axial behavior and micromechanics of trabecular bone subjected to various loading conditions. A new multi-axial yield criterion of human trabecular bone has been proposed. In particular, decoupling the uniaxial strength behavior from the multi-axial strength behavior eliminated the effects of bone volume fraction, anisotropy and microarchitecture on the multi-axial strength.

6. REFERENCES

1. Morgan, E.F., H.H. Bayraktar, and T.M. Keaveny, Trabecular bone modulus-density relationships depend on anatomic site. Journal of Biomechanics, 2003. **36**(7): p. 897-904.
2. Odgaard, A., Three-dimensional methods for quantification of cancellous bone architecture. Bone, 1997. **20**(4): p. 315-28.
3. Cowin, S.C., The relationship between the elasticity tensor and the fabric tensor. Mechanics of Materials, 1985. **4**: p. 137-147.
4. Whitehouse, W.J., The quantitative morphology of anisotropic trabecular bone. Journal of Microscopy, 1974. **2**: p. 153-68.
5. Harrigan, T. and R. Mann, Characterization of microstructural anisotropy in orthotropic materials using a second rank tensor. Journal of Material Science, 1984. **19**: p. 761-767.
6. Zysset, P.K., A review of morphology-elasticity relationships in human trabecular bone: theories and experiments. Journal of Biomechanics, 2003. **36**(10): p. 1469-85.
7. Cowin, S., ed. Bone Mechanics Handbook. 2 ed. 2001, CRC Press: Boca Raton. 968.
8. Hildebrand, T. and P. Ruegsegger, Quantification of Bone Microarchitecture with the Structure Model Index. Computer Methods Biomechanics and Biomedical Engineering, 1997. **1**(1): p. 15-23.
9. Rüegsegger, P., B. Koller, and R. Müller, A microtomographic system for the nondestructive evaluation of bone architecture. Calcified Tissue International, 1996. **58**(1): p. 24-9.
10. Hildebrand, T., et al., Direct three-dimensional morphometric analysis of human cancellous bone: microstructural data from spine, femur, iliac crest, and calcaneus. Journal of Bone and Mineral Research, 1999. **14**(7): p. 1167-74.
11. Liu, S., et al., Complete Volumetric Decomposition of Individual Trabecular Plates and Rods and Its Morphological Correlations with Anisotropic Elastic Moduli in Human Trabecular Bone x. Journal of Bone and Mineral Research, 2008. **23**(2): p. 223-35.
12. Cowin, S.C. and C.H. Turner, On the relationship between the orthotropic Youngs Moduli and Fabric. Journal of Biomechanics, 1992. **25**(12): p. 1493-1494.
13. Ciarelli, M.J., et al., Evaluation of Orthogonal Mechanical-Properties and Density of Human Trabecular Bone from the Major Metaphyseal Regions with Materials Testing and Computed-Tomography. Journal of Orthopaedic Research, 1991. **9**(5): p. 674-682.
14. Morgan, E.F. and T.M. Keaveny, Dependence of yield strain of human trabecular bone on anatomic site. Journal of Biomechanics, 2001. **34**(5): p. 569-577.
15. Rice, J.C., S.C. Cowin, and J.A. Bowman, On the dependence of the elasticity and strength of cancellous bone on apparent density. Journal of Biomechanics, 1988. **21**(2): p. 155-168.
16. Matsuura, M., et al., The role of fabric in the quasi-static compressive mechanical properties of human trabecular bone from various anatomical locations. Biomechanics and Modeling in Mechanobiology, 2008. **7**(1): p. 27-42.

17. Kopperdahl, D.L. and T.M. Keaveny, Yield strain behavior of trabecular bone. Journal of Biomechanics, 1998. **31**(7): p. 601-8.
18. Bevill, G., F. Farhamand, and T.M. Keaveny, Heterogeneity of yield strain in low-density versus high-density human trabecular bone. Journal of Biomechanics, 2009. **42**(13): p. 2165-70.
19. Fenech, C.M. and T.M. Keaveny, A cellular solid criterion for predicting the axial-shear failure properties of trabecular bone. Journal of Biomechanical Engineering, 1999. **121**: p. 414-422.
20. Tsai, S. and E. Wu, A general theory for strength of anisotropic materials. Journal of Composite Materials, 1971. **5**: p. 58-80.
21. Cowin, S.C., Fabric dependence of an anisotropic strength criterion. Mechanics of Materials, 1986. **5**: p. 251-260.
22. Keaveny, T.M., et al., Application of the Tsai-Wu quadratic multiaxial failure criterion to bovine trabecular bone. Journal of Biomechanical Engineering, 1999. **121**: p. 99-107.
23. Niebur, G.L., M.J. Feldstein, and T.M. Keaveny, Biaxial failure behavior of bovine tibial trabecular bone. Journal of Biomechanical Engineering, 2002. **124**(6): p. 699-705.
24. Bayraktar, H.H., et al., The modified super-ellipsoid yield criterion for human trabecular bone. Journal of Biomechanical Engineering, 2004. **126**(6): p. 677-84.
25. Zysset, P.K. and L. Rincon-Kohli, An alternative fabric-based yield and failure criterion for trabecular bone. In: Holzapfel GA, Ogden RW (eds) Mechanics of biological tissue., 2006: p. 457-470.
26. Rincon-Kohli, L. and P.K. Zysset, Multi-axial mechanical properties of human trabecular bone. Biomechanics and Modeling in Mechanobiology, 2009. **8**(3): p. 195-208.
27. Wolfram, U., et al., Fabric-based Tsai-Wu yield criteria for vertebral trabecular bone in stress and strain space. Journal of Mechanical Behavior of Biomedical Materials, 2012. **15**: p. 218-28.
28. Gibson, L.J., et al., Failure surfaces for cellular materials under multiaxial loads-I. Modelling. International Journal of Mechanical Sciences, 1989. **31**(9): p. 635-663.
29. Deshpande, V.S. and N.A. Fleck, Multi-axial Yield Behavior of Polymer Foams. Acta Materialia, 2001. **49**: p. 1859-1866.
30. Kelly, N. and J.P. McGarry, Experimental and numerical characterisation of the elasto-plastic properties of bovine trabecular bone and a trabecular bone analogue. Journal of Mechanical Behavior of Biomedical Materials, 2012. **9**: p. 184-97.
31. Carter, D.R. and W.C. Hayes, Bone compressive strength: the influence of density and strain rate. Science, 1976. **194**(4270): p. 1174-6.
32. Goldstein, S.A., The mechanical properties of trabecular bone: dependence on anatomic location and function. Journal of Biomechanics, 1987. **20**(11/12): p. 1055-1061.
33. Goulet, R.W., et al., The relationship between the structural and orthogonal compressive properties of trabecular bone. Journal of Biomechanics, 1994. **27**(4): p. 375-389.
34. Keller, T.S., Predicting the Compressive Mechanical-Behavior of Bone. Journal of Biomechanics, 1994. **27**(9): p. 1159-1168.

35. Ford, C.M. and T.M. Keaveny, The dependence of shear failure properties of bovine tibial trabecular bone on apparent density and trabecular orientation. Journal of Biomechanics, 1996. **29**(10): p. 1309-1317.
36. Keyak, J.H., Relationships between femoral fracture loads for two load configurations. Journal of Biomechanics, 2000. **33**(4): p. 499-502.
37. Lotz, J.C., E.J. Cheal, and W.C. Hayes, Fracture prediction for the proximal femur using finite element models: Part II--Nonlinear analysis. Journal of Biomechanical Engineering, 1991. **113**(4): p. 361-365.
38. Cheal, E.J., M. Spector, and W.C. Hayes, Role of loads and prosthesis material properties on the mechanics of the proximal femur after total hip arthroplasty. Journal of Orthopaedic Research, 1992. **10**(3): p. 405-22.
39. Bruyere Garnier, K., et al., Mechanical characterization in shear of human femoral cancellous bone: torsion and shear tests. Medical Engineering & Physics, 1999. **21**(9): p. 641-9.
40. Halawa, M., et al., The shear strength of trabecular bone from the femur, and some factors affecting the shear strength of the cement-bone interface. Arch Orthop Trauma Surg, 1978. **92**(1): p. 19-30.
41. Kasra, M. and M.D. Grynpas, On shear properties of trabecular bone under torsional loading: effects of bone marrow and strain rate. Journal of Biomechanics, 2007. **40**(13): p. 2898-903.
42. Mitton, D., et al., The effects of density and test conditions on measured compression and shear strength of cancellous bone from the lumbar vertebrae of ewes. Medical Engineering & Physics, 1997. **19**(5): p. 464-74.
43. Stone, J.L., G.S. Beaupre, and W.C. Hayes, Multiaxial strength characteristics of trabecular bone. Journal of Biomechanics, 1983. **16**(9): p. 743-52.
44. Garrison, J.G., J.A. Gargac, and G.L. Niebur, Shear strength and toughness of trabecular bone are more sensitive to density than damage. Journal of Biomechanics, 2011. **44**(16): p. 2747-54.
45. Ciarelli, T.E., et al., Variations in three-dimensional cancellous bone architecture of the proximal femur in female hip fractures and in controls. Journal of Bone and Mineral Research, 2000. **15**(1): p. 32-40.
46. Homminga, J., et al., The osteoporotic vertebral structure is well adapted to the loads of daily life, but not to infrequent "error" loads. Bone, 2004. **34**(3): p. 510-6.
47. Bevill, G., et al., Influence of bone volume fraction and architecture on computed large-deformation failure mechanisms in human trabecular bone. Bone, 2006. **39**(6): p. 1218-25.
48. Beck, J.D., et al., Three-dimensional imaging of trabecular bone using the computer numerically controlled milling technique. Bone, 1997. **21**(3): p. 281-7.
49. Laib, A., et al. Direct measures of trabecular bone architecture from MR images. in Noninvasive assessment of trabecular bone architecture and the competence of bone. 2001. Big Sur, California: Kluwer Academic/Plenum Publishers.
50. Guldberg, R.E., S.J. Hollister, and G.T. Charras, The accuracy of digital image-based finite element models. Journal of Biomechanical Engineering, 1998. **120**(4): p. 289-295.

51. Niebur, G.L., et al., Convergence behavior of high-resolution finite element models of trabecular bone. Journal of Biomechanical Engineering, 1999. **121**(6): p. 629-635.
52. van Rietbergen, B., et al., Direct mechanics assessment of elastic symmetries and properties of trabecular bone architecture. Journal of Biomechanics, 1996. **29**(12): p. 1653-1657.
53. Papadopoulos, P. and J. Lu, On the formulation and numerical solution of problems in anisotropic finite plasticity. Computer Methods in Applied Mechanics and Engineering, 2001. **190**(37-38): p. 4889-4910.
54. Adams, M.F., et al. Ultrascalable implicit finite element analyses in solid mechanics with over a half a billion degrees of freedom. in ACM/IEEE Proceedings of SC2004: High Performance Networking and Computing. 2004.
55. Nádai, A., Theory of flow and fracture of solids. Engineering societies monographs1950, New York,: McGraw-Hill.
56. Stolken, J.S. and J.H. Kinney, On the importance of geometric nonlinearity in finite-element simulations of trabecular bone failure. Bone, 2003. **33**(4): p. 494-504.
57. Saha, S. and P.H. Gorman. Strength of human cancellous bone in shear and its relationship to bone mineral content. in Transactions of Orthopaedic Research Society. 1981.
58. Arlot, M.E., et al., Microarchitecture influences microdamage accumulation in human vertebral trabecular bone. Journal of Bone and Mineral Research, 2008. **23**(10): p. 1613-8.
59. Karim, L. and D. Vashishth, Role of trabecular microarchitecture in the formation, accumulation, and morphology of microdamage in human cancellous bone. Journal of Orthopaedic Research, 2011. **29**(11): p. 1739-1744.
60. Fyhrie, D.P. and M.B. Schaffler, Failure mechanisms in human vertebral cancellous bone. Bone, 1994. **15**(1): p. 105-9.
61. Nagaraja, S., T.L. Couse, and R.E. Guldberg, Trabecular bone microdamage and microstructural stresses under uniaxial compression. Journal of Biomechanics, 2005. **38**(4): p. 707-16.
62. Shi, X., et al., Effects of trabecular type and orientation on microdamage susceptibility in trabecular bone. Bone, 2010. **46**(5): p. 1260-6.
63. Wegrzyn, J., et al., Role of trabecular microarchitecture and its heterogeneity parameters in the mechanical behavior of ex vivo human L3 vertebrae. Journal of Bone and Mineral Research, 2010. **25**(11): p. 2324-31.
64. Yeh, O.C. and T.M. Keaveny, Biomechanical effects of intraspecimen variations in trabecular architecture: A three-dimensional finite element study. Bone, 1999. **25**(2): p. 223-228.
65. Yeni, Y.N., et al., Variability of trabecular microstructure is age-, gender-, race- and anatomic site-dependent and affects stiffness and stress distribution properties of human vertebral cancellous bone. Bone, 2011. **49**(4): p. 886-94.
66. Bourne, B.C. and M.C. van der Meulen, Finite element models predict cancellous apparent modulus when tissue modulus is scaled from specimen CT-attenuation. Journal of Biomechanics, 2004. **37**(5): p. 613-21.

67. Gross, T., et al., Mineral heterogeneity has a minor influence on the apparent elastic properties of human cancellous bone: a SRμCT-based finite element study. Computer Methods in Biomechanics and Biomedical Engineering, 2012. **15**(11): p. 1137-44.
68. Jaasma, M.J., et al., Biomechanical effects of intraspecimen variations in tissue modulus for trabecular bone. Journal of Biomechanics, 2002. **35**(2): p. 237-246.
69. Verhulp E, V.R.B., Muller R, Huiskes R, Micro-finite element simulation of trabecular-bone post-yield behaviour--effects of material model, element size and type. Computer Methods in Biomechanics and Biomedical Engineering, 2008. **11**(4): p. 389-95.
70. Carnelli, D., et al., A finite element model for direction-dependent mechanical response to nanoindentation of cortical bone allowing for anisotropic post-yield behavior of the tissue. Journal of Biomechanical Engineering, 2010. **132**(8): p. 081008.
71. Schwiedrzik, J.J. and P.K. Zysset, An anisotropic elastic-viscoplastic damage model for bone tissue. Biomechanics and Modeling in Mechanobiology, 2013. **12**(2): p. 201-13.
72. Pahr, D.H. and P.K. Zysset, Influence of boundary conditions on computed apparent elastic properties of cancellous bone. Biomechanics and Modeling in Mechanobiology, 2008. **7**(6): p. 463-76.
73. Bevill, G., et al., The influence of boundary conditions and loading mode on high-resolution finite element-computed trabecular tissue properties. Bone, 2009. **44**(4): p. 573-8.
74. Van Rietbergen, B., et al., Trabecular bone tissue strains in the healthy and osteoporotic human femur. Journal of Bone and Mineral Research, 2003. **18**(10): p. 1781-1788.
75. Verhulp, E., B. van Rietbergen, and R. Huiskes, Load distribution in the healthy and osteoporotic human proximal femur during a fall to the side. Bone, 2008. **42**(1): p. 30-5.
76. Newitt, D.C., et al., In vivo assessment of architecture and micro-finite element analysis derived indices of mechanical properties of trabecular bone in the radius. Osteoporosis International, 2002. **13**(1): p. 6-17.
77. Tanck, E., et al., Predictive value of femoral head heterogeneity for fracture risk. Bone, 2009. **44**(4): p. 590-5.
78. Homminga, J., et al., Cancellous bone mechanical properties from normals and patients with hip fractures differ on the structure level, not on the bone hard tissue level. Bone, 2002. **30**(5): p. 759-64.
79. Sanyal, A., et al., Shear strength behavior of human trabecular bone. Journal of Biomechanics, 2012. **45**(15): p. 2513-9.
80. Fitzgibbon, A., P. M, and B. Fisher, Direct least-squares fitting of ellipses. IEEE Transactions on Pattern Analysis and Machine Intelligence, 1999. **21**(5): p. 476-480.
81. Mosekilde, L., Age-related changes in vertebral trabecular bone architecture--assessed by a new method. Bone, 1988. **9**(4): p. 247-50.

82. Thomsen, J.S., E.N. Ebbesen, and L. Mosekilde, Age-related differences between thinning of horizontal and vertical trabeculae in human lumbar bone as assessed by a new computerized method. Bone, 2002. **31**(1): p. 136-142.
83. Wu, R. and Z. Stachurski, Evaluation of the Normal Stress Interaction Parameter in the Tensor Polynomial Strength Theory for Anisotropic Materials. Journal of Composite Materials, 1984. **18**: p. 456-463.
84. Traintafillou, T.C., et al., Failure surfaces for cellular materials under multiaxial loads. II. Comparison of models with experiment. International Journal of Mechanical Sciences, 1989. **31**(9): p. 665-78.
85. D.A. Wang, J.P., A non-quadratic yield function for polymeric foams. International Journal of Plasticity, 2006. **22**: p. 434–458.
86. Cezayirlioglu, H., et al., Anisotropic yield behavior of bone under combined axial force and torque. Journal of Biomechanics, 1985. **18**(1): p. 61-9.
87. Gioux, G., T.M. McCormack, and L.J. Gibson, Failure of aluminium foams under multiaxial loads. International Journal of Mechanical Sciences, 2000. **42**: p. 1097-1117.
88. Rottler, J. and M.O. Robbins, Yield Conditions for deformation of amorphous polymer glasses. Physical Review E, 2001. **64**: p. 051801-1-8.
89. Brezny, R. and D.J. Green, Characterization of edge effects In cellular materials. Journal of Materials Science, 1990. **25**(11): p. 4571-4578.
90. Turner, C.H. and S.C. Cowin, Errors introduced by off-axis measurements of the elastic properties of bone. Journal of Biomechanics, 1988. **110**: p. 213-214.
91. Triantafillou, T.C. and L.J. Gibson, Multiaxial failure criteria for brittle foams. International Journal of Mechanical Sciences, 1990. **32**(6): p. 479-496.
92. Burr, D.B., The contribution of the organic matrix to bone's material properties. Bone, 2002. **31**(1): p. 8-11.
93. Milovanovic, P., et al., Age-related deterioration in trabecular bone mechanical properties at material level: nanoindentation study of the femoral neck in women by using AFM. Experimental Gerontology, 2012. **47**(2): p. 154-9.
94. Kabel, J., et al., The role of an effective isotropic tissue modulus in the elastic properties of cancellous bone. Journal of Biomechanics, 1999. **32**(7): p. 673-80.
95. Hou, F.J., et al., Human vertebral body apparent and hard tissue stiffness. Journal of Biomechanics, 1998. **31**(11): p. 1009-15.
96. Easley, S.K., et al., Contribution of the intra-specimen variations in tissue mineralization to PTH- and raloxifene-induced changes in stiffness of rat vertebrae. Bone, 2010. **46**(4): p. 1162-9.
97. Wang, C., L. Feng, and I. Jasiuk, Scale and boundary conditions effects on the apparent elastic moduli of trabecular bone modeled as a periodic cellular solid. J Biomech Eng, 2009. **131**(12): p. 121008.
98. Vasu, R., D.R. Carter, and W.H. Harris, Stress distributions in the acetabular region. I. Before and after total joint replacement. Journal of Biomechanics, 1981. **15**: p. 155-164.
99. Carter, D.R., T.E. Orr, and D.P. Fyhrie, Relationships between loading history and femoral cancellous bone architecture. Journal of Biomechanics, 1989. **22**(3): p. 231-44.

100. Garcia, D., et al., A three-dimensional elastic plastic damage constitutive law for bone tissue. Biomechanics and Modeling in Mechanobiology, 2009. **8**(2): p. 149-65.
101. Dall'Ara, E., et al., QCT-based finite element models predict human vertebral strength in vitro significantly better than simulated DEXA. Osteoporosis International, 2012. **23**(2): p. 563-72.
102. Chevalier, Y., D. Pahr, and P.K. Zysset, The role of cortical shell and trabecular fabric in finite element analysis of the human vertebral body. Journal of Biomechanical Engineering, 2009. **131**(11): p. 111003.
103. Gibson, L.J., Biomechanics of cellular solids. Journal of Biomechanics, 2005. **38**(3): p. 377-99.
104. Gibson, L.J. and M.F. Ashby, The mechanics of three-dimensional cellular materials. Proc. R. Soc. (London), 1982. **382**: p. 43-59.
105. Gibson, L.J., The mechanical behavior of cancellous bone. Journal of Biomechanics, 1985. **18**(5): p. 317-328.
106. Gdoutos, E.E., I.M. Daniel, and K.-A. Wang, Failure of cellular foams under multiaxial loading. Composites: Part A, 2002. **33**: p. 163-176.
107. Zaslawsky, M., Multiaxial-stress studies on rigid polyurethane foam. Experimental Mechanics, 1973. **2**(Feb): p. 70-76.
108. Charras, G.T. and R.E. Guldberg, Improving the local solution accuracy of large-scale digital image-based finite element analyses. Journal of Biomechanics, 2000. **33**(2): p. 255-9.
109. Walker, J.D. and B.H. Thacker. Yield surfaces for anisotropic plates. American Institute of Physics. 1999. Snowbird, Utah (USA).
110. Barlat, F., D.J. Lege, and J.C. Brem, A six-component yield function for anisotropic materials. International Journal of Plasticity, 1991. **7**: p. 693-712.
111. Karafillis, A.P. and M.C. Boyce, A general anisotropic yield criterion using bounds and a transformation weighting tensor. Journal of the Mechanics and Physics of Solids, 1993. **41**(12): p. 1859-1886.
112. Gol'denblat, I.I. and V.A. Kopnov, Strength of glass-reinforced plastics in the complex stress state. Polymer Mechanics, 1965. **1**(2): p. 54-59.
113. von Mises, R., Mechanik der Plastischen Formaenderung von Kristallen. Zeitschrift fuer Angewandte Mathematik und Mechnik, 1928. **8**: p. 161-185.
114. Hill, R., The mathematical theory of plasticity. Oxford engineering science series1983, Oxford New York: Clarendon Press ; Oxford Univerity Press. ix, 355.
115. Hoffman, O., The brittle strength of orthotropic materials. Journal of Composite Materials, 1967. **1**: p. 200-206.
116. Schwiedrzik, J.J., U. Wolfram, and P.K. Zysset, A generalized anisotropic quadric yield criterion and its application to bone tissue at multiple length scales. Biomechanics and Modeling in Mechanobiology, 2013.
117. Bower, M.V. and D.H. Koedam, Tensor Polynomial Failure Criterion: Coefficient Limits Based on Convexity Requirements. Journal of Reinforced Plastics and Composites, 1997. **16**(5): p. 435-477.
118. Bevill, G., S.K. Easley, and T.M. Keaveny, Side-artifact errors in yield strength and elastic modulus for human trabecular bone and their dependence on bone

volume fraction and anatomic site. Journal of Biomechanics, 2007. **40**(15): p. 3381-8.
119. He, Q.-C., Effects of size and boundary conditions on the yield strength of heterogeneous materials. Journal of the Mechanics and Physics of Solids, 2001. **49**: p. 2557 – 2575.
120. Rowlands, R.E., Strength (failure) theories and their experimental correlations, in Handbook of Composites, Volume 3, G.C. Sih and A.M. Skudra, Editors. 1985, Elsevier Science: Amsterdam. p. 71-125.
121. Keaveny, T.M., et al., Differences between the tensile and compressive strengths of bovine tibial trabecular bone depend on modulus. Journal of Biomechanics, 1994. **27**: p. 1137-1146.
122. Hardisty, M.R., et al., The importance of intrinsic damage properties to bone fragility: a finite element study. Journal of Biomechanical Engineering, 2013. **135**(1): p. 011004.
123. Carretta, R., et al., Within subject heterogeneity in tissue-level post-yield mechanical and material properties in human trabecular bone. Journal of Mechanical Behavior of Biomedical Materials, 2013. **24**: p. 64-73.
124. Nagaraja, S., O. Skrinjar, and R.E. Guldberg, Spatial correlations of trabecular bone microdamage with local stresses and strains using rigid image registration. Journal of Biomechanical Engineering, 2011. **133**(6): p. 064502.
125. Niebur, G.L., et al., High-resolution finite element models with tissue strength asymmetry accurately predict failure of trabecular bone. Journal of Biomechanics, 2000. **33**: p. 1575-1583.
126. Keaveny, T.M., et al., Systematic and random errors in compression testing of trabecular bone. Journal of Orthopaedic Research, 1997. **15**: p. 101-110.

7. APPENDIX

Introduction

High-resolution micro-CT based finite element modeling provides an accurate reconstruction of bone trabecular microstructure and has been widely used to assess bone strength *in-silico* [24, 96, 125]. While the yield strength estimates from these models have been validated for uniaxial compression loading [47, 79], the fidelity of these models to predict strength under multi-axial loading is still an open question. The overall goal of this study was to establish validity of high-resolution nonlinear finite element models for strength prediction of cylindrical cores of trabecular bone subjected to multi-axial loading.

Methods

Fifteen cylindrical cores of human femoral neck trabecular bone (~8 mm diameter, 25 mm length) were taken from 15 donors (age=69±8, 52-81 years; n=10 male, n=5 female) with a wide range of bone volume fraction (BV/TV = 0.29±0.06, 0.17-0.38). All specimens were cored such that the main trabecular orientation was aligned with the axis of the cylinder [14]. Specimens were kept hydrated, wrapped in plastic, and stored at -20^0C in airtight containers until mechanical testing. Before mechanical testing, specimens were taken out of the freezer and thawed. Then, the two ends of each specimen (around 3-4 mm) were submerged in 10% bleach solution to dissolve the bone marrow. The specimen was then water jet to remove any remaining bone marrow followed by air jetting the ends. For mechanical testing, each specimen core was affixed in brass endcaps to avoid end-artifacts [126]. Circular wells (~2 mm deep, and 10 mm diameter) were machined at one end of a solid brass rod and specimens were affixed in the wells using PMMA while being held in a custom jig to ensure that the endcaps were aligned. Before testing, the total length, diameter, and exposed length of bone between the end-caps were measured. All tests were performed in strain control at room temperature using a servohydraulic axial-torsion load frame (858 mini-bionix, MTS, Eden Prairie, MN) equipped with a multiaxial load cell (**Figure A1**). First, non-destructive testing was performed for each specimen under compression (to 0.2% apparent strain) and torsion (to 0.4% engineering shear strain). A 25 mm gage length axial extensometer, attached to the end-caps, was used to measure axial displacement, and the load frame rotational variable displacement transducer was used to measure angle-of-twist. After non-destructive testing was completed, specimens were tested to failure in either uniaxial loading: compression (n=1), tension (n=1), torsion (n=1), or multiaxial loading: combined compression-torsion (n=6), combined tension-torsion (n=6). For the multiaxial loading cases, the ratio of shear to axial strains (and strain rates) was kept constant during each combined axial-torsion test.

Prior to mechanical testing, each specimen was micro-CT scanned at an isotropic spatial resolution 10 μm. Images were coarsened to 20 μm using a region-averaging technique. High-resolution finite element models were created from each image that explicitly modeled the experimental boundary conditions specific for each specimen. A linear

elastic finite element analyses were performed for each specimen to simulate non-destructive mechanical testing in compression and torsion, and the effective trabecular tissue elastic modulus was computed by comparing the slope of the force-deformation or torque-theta curve with experiment. Nonlinear finite element analyses was performed for each specimen with axial and torsion strain boundary conditions applied in the same proportion as applied in the experiments. For the nonlinear analysis, trabecular tissue was assumed to an elastic-plastic material with von Mises yielding with tissue strength asymmetry as assumed in Chapters 2, 3 and 4. The force-vs-displacement curve was used to calculate the axial stress-strain response. The torque-vs-angle of twist curve was used to calculate the shear stress-strain response as described in chapter 2. The yield stress and strain were calculated individually for the axial and shear response. The first direction to yield was used to define the chronological yield point.

Results

The effective tissue elastic modulus measured from the non-destructive compression and torsion tests was 18.9±2.4 GPa (14.1-22.0 GPa). Under combined tension-torsion loading, most specimens broke near the endcaps (**Figure A1**), whereas under compression-torsion loading, the specimens broke somewhere in the middle. Under combined loading, failure first occurred in the axial direction unless the applied torsion load was very high.

The distribution of yield strains obtained from experiments and yield strains computed from the respective finite element analyses, had a good agreement for some specimens but had a significant difference for other specimens (**Figure A2**). In addition, the predicted mode of yield (axial v/s torsion) was not in agreement for most of the specimens. While the yield point predicted from the stress-strain response of the finite element models was in close agreement with the experimentally obtained yield point, the finite element models did not capture the post-yield response such as strain softening especially in the torsion mode (**Figure A3**).

Conclusion

Although high-resolution finite element models have been widely used to predict the strength of both cylindrical cores of trabecular bone and whole bone, the results of this study shows that the validity of such models is still inconclusive under multi-axial loading. This could be due to errors introduced in the experiments. Due to machine compliance and due to the presence of a layer of PMMA around the perimeter of the bone in the brass endcaps, we suspect the angle of twist measurements may not have been accurate. We designed the new endcaps to accommodate a thin layer of PMMA around the bone specimen to avoid slipping of the specimen within the endcaps during testing. Also, due to heterogeneous nature of trabecular bone structure, there could have been local failure within the trabecular structure before the overall failure, which could have caused variations in the force and torque responses. Future research can involve designing new endcaps, testing specimens from other anatomic sites and investigating other material models that capture the post-yield strain softening response.

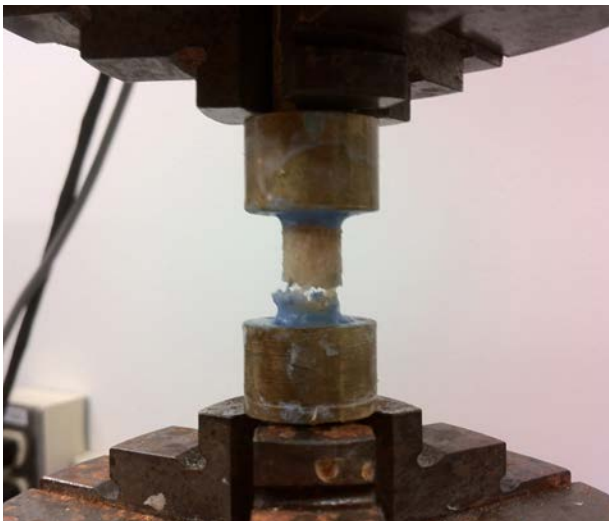

Figure A1. A broken specimen tested under combined tension-torsion after testing.

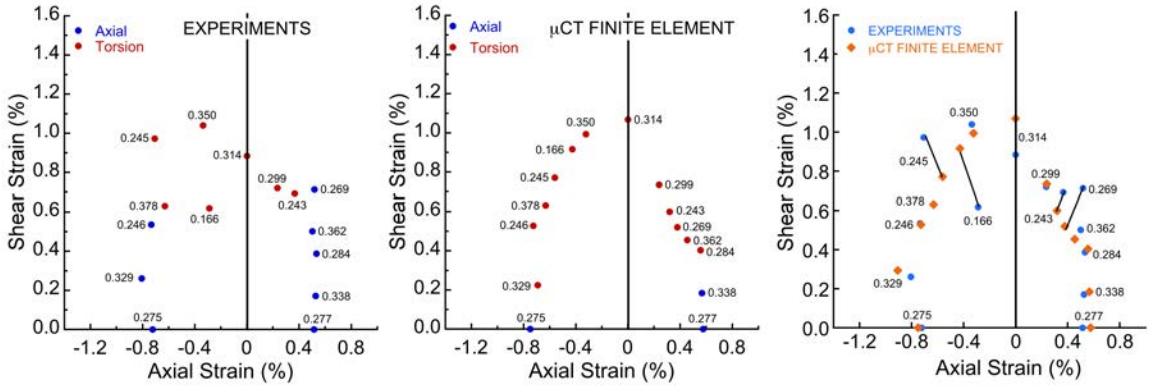

Figure A2. Distribution of yield points obtained from experiments (*left*) and non-linear finite element analysis (*middle*). A red mark indicates chronological yield in torsion whereas blue mark indicates chronological yield in tension/compression. The data points from experiments and finite element analysis are plotted together on the right-hand chart. The values shown are the BV/TV of specimens.

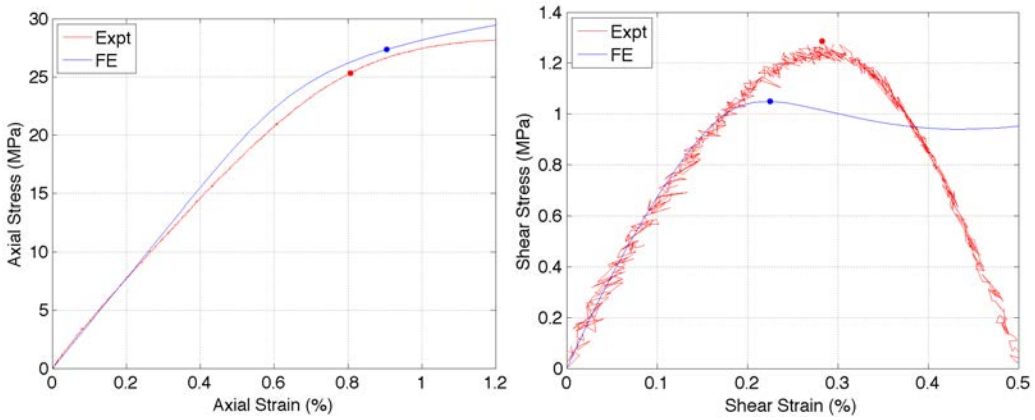

Figure A3. Experimentally obtained and finite element computed axial stress-strain response (*left*) and torsional shear stress-stress response (*right*) for a specimen subjected to a combined compression-torsion loading (BVTV = 0.329). The highlighted point on each curve is the yield point obtained using a 0.2% strain offset.